Research Square

Preprints are preliminary reports that have not undergone peer review.
They should not be considered conclusive, used to inform clinical practice,
or referenced by the media as validated information.

SPP1+ Macrophage-T Cell Axis Orchestrates the Immune Microenvironment in Breast Cancer Bone Metastasis

Zixue Xuan

xuanzixue0222@163.com

Department of Pharmacy, Zhejiang Provincial People's Hospital Bijie Hospital, Bijie, Guizhou, China;

Zhongxiu Wu

Center for Clinical Pharmacy, Cancer Center, Department of Pharmacy, Zhejiang Provincial People's Hospital (Affiliated People's Hospital), Hangzhou Medical College, Hangzhou, Zhejiang, China

Yuting Zhong

Hangzhou Medical College, Hangzhou, Zhejiang, China;

Jinying Jiang

Department of Pharmacy, Zhejiang Provincial People's Hospital Bijie Hospital, Bijie, Guizhou, China;

Yuan Zhang

Center for Clinical Pharmacy, Cancer Center, Department of Pharmacy, Zhejiang Provincial People's Hospital (Affiliated People's Hospital), Hangzhou Medical College, Hangzhou, Zhejiang, China

Lei Cheng

Center for Clinical Pharmacy, Cancer Center, Department of Pharmacy, Zhejiang Provincial People's Hospital (Affiliated People's Hospital), Hangzhou Medical College, Hangzhou, Zhejiang, China

Jun Zhang

Department of Orthopedics, Zhejiang Provincial People’s Hospital Bijie Hospital, Bijie, Guizhou, China;

Kai Wang

Key Laboratory of Epigenetics and Oncology, Research Center for Preclinical Medicine, Southwest Medical University, Luzhou, China.

Research Article

Keywords: breast cancer, bone metastasis, immune microenvironment, Mac-SPP1

Posted Date: March 4th, 2026

DOI: https://doi.org/10.21203/rs.3.rs-8805630/v1

License: This work is licensed under a Creative Commons Attribution 4.0 International License.
Read Full License

Additional Declarations: No competing interests reported.

SPP1+ Macrophage-T Cell Axis Orchestrates the Immune Microenvironment in Breast Cancer Bone Metastasis

Zixue Xuan[1,2,#,*], Zhongxiu Wu[1,#], Yuting Zhong[3], Jinying Jiang[1,2], Yuan Zhang[1], Lei Cheng[1], Jun Zhang[4,5,*], Kai Wang[6,*]

1 Department of Pharmacy, Zhejiang Provincial People's Hospital Bijie Hospital, Bijie, Guizhou, China;

2 Center for Clinical Pharmacy, Cancer Center, Department of Pharmacy, Zhejiang Provincial People's Hospital (Affiliated People's Hospital), Hangzhou Medical College, Hangzhou, Zhejiang, China;

3 Hangzhou Medical College, Hangzhou, Zhejiang, China;

4 Department of Orthopedics, Zhejiang Provincial People's Hospital Bijie Hospital, Bijie, Guizhou, China;

5 Center for Plastic & Reconstructive Surgery, Department of Orthopedics, Zhejiang Provincial People's Hospital (Affiliated People's Hospital), Hangzhou Medical College, Hangzhou, Zhejiang, China;

6 Key Laboratory of Epigenetics and Oncology, Research Center for Preclinical Medicine, Southwest Medical University, Luzhou, China.

Co-first authors

* Corresponding author. Zixue Xuan, Jun Zhang, Kai Wang; Email: xuanzixue0222@163.com (ZX.X); spinecarezhangjun@163.com (J.Z), wangkai@swmu.edu.cn (K.W).

Abstract

Background Breast cancer is a highly common malignancy in women, with bone as its most frequent site of distant metastasis, significantly increasing mortality risk.

Methods This study integrated single-cell RNA sequencing datasets (GSE266330 and GSE243526) to systematically characterize the dynamic evolution of the tumor microenvironment from normal tissue to primary tumor and bone metastasis in breast cancer.

Results In total, 141,056 high-quality single cells were analyzed, identifying 11 major cell types. Myeloid cell and T cell proportions were significantly elevated in bone metastases, suggesting their pivotal role in metastatic progression. The bone metastasis-enriched Mac-SPP1 macrophage subpopulation exhibited M2 polarization, high metabolic activity, and a significant association with poor patient prognosis (P = 4.9e-05). It highly expressed transcription factors such as HOXA9 and MAF, potentially promoting metastasis through regulation of an immunosuppressive network. Among T cells, the CD4-S100A9 and CD8-GZMK subpopulations were significantly expanded in bone metastases and exhibited high cytotoxicity, high exhaustion, and metabolic reprogramming. Pseudotime analysis showed that CD4-S100A9 cells were at the initial state of CD4+ T cell differentiation, whereas CD8-GZMK cells serve a key transitional node from effector memory toward exhaustion. Cell-cell communication analysis revealed that Mac-SPP1 interact specifically with these CD4/CD8 T cell subsets through the SPP1-integrin axis (e.g., SPP1-CD44) and the CD74-MIF/COPA signaling axis, potentially driving T cell functional exhaustion and immune evasion.

Conclusion This study is the first to delineate the synergistic pro-metastatic role of the Mac-SPP1–CD4-S100A9/CD8-GZMK axis in breast cancer bone metastasis, providing a theoretical basis for developing therapeutic strategies targeting the immune microenvironment.

Keywords breast cancer; bone metastasis; immune microenvironment; Mac-SPP1

Introduction

Breast cancer is a highly common malignancy in women globally, holding the highest incidence rate and ranking as the fifth most common cause of cancer mortality worldwide [1]. Bone is the most common site of metastasis in breast cancer [2], and the occurrence of bone metastasis in breast cancer significantly increases mortality risk, highlighting the urgent need for focused research and intervention in the treatment of breast cancer [3]. Numerous studies have revealed that the tumor microenvironment, particularly specific cell subpopulations, plays a pivotal role in breast cancer bone metastasis. For instance, tumor-derived granulocyte colony-stimulating factor modulates the bone marrow vascular microenvironment [4]; proline dehydrogenase 2 influences hydroxyproline metabolism and promotes SLC7A11 and CXCL8 expression [5]; the 5-methylcytosine methyltransferase NSUN2 accelerates the degradation of lysine demethylase 6B mRNA, thereby activating the Notch signaling pathway and increasing RANKL expression [6]; and the N6-methyladenosine reader YTHDF3 enhances the translation of ZEB1 and SMAD5 [7]. All these mechanisms help promote breast cancer bone metastasis, illustrating the high complexity of the mechanisms driving breast-cancer bone metastasis. Thus, further studies are still needed to elucidate such mechanisms.

Advances in single-cell RNA sequencing (scRNA-seq) technology have enabled accurate and in-depth studies of the tumor microenvironment and cellular heterogeneity [8], thereby uncovering the mechanisms underlying breast cancer bone metastasis. Kaur J et al. identified transcriptomic alterations in senescent osteocytes in a mouse model of breast cancer bone metastasis, and another study showed that SCUBE2 is enriched in osteoblastic subpopulations of the early bone-metastatic niche, suggesting a potential role in driving “seed-and-soil” interactions [9]. Wang et al. further showed that lymphotoxin-β (LTβ) is highly expressed by tumor cells in the bone microenvironment, fostering their colonization and growth [10]. Complementing these findings, a recent study mapped the single-cell landscape of primary breast tumors and adjacent normal tissue [11], while a second, large-scale atlas profiled 42 bone metastases across eight solid-tumor types, providing the first cross-cancer comparison of shared and tumor-

specific bone-metastatic programs, with breast cancer samples being a major component [12].

By integrating these two recent and complementary datasets, the present study aimed to systematically dissect the cellular heterogeneity along the “normal-primary tumor-bone metastasis” trajectory, identify key subpopulations and molecular switches that drive bone metastasis, and propose a targetable “metastasis-specific” cellular blueprint for future therapeutic intervention strategies. The findings of this study clarify the cellular heterogeneity of breast cancer bone metastasis and provide an important scientific basis for developing effective prevention and treatment strategies.

Methods

scRNA-seq data sources

scRNA-seq data were obtained from GSE266330 (including 12 breast cancer bone metastasis samples) [12] and GSE243526 [11] (including 8 primary tumors and 4 normal samples), which were downloaded from the Gene Expression Omnibus (GEO) database (https://www.ncbi.nlm.nih.gov/geo/). The transcriptome and clinical data of breast cancer were retrieved from The Cancer Genome Atlas Breast Invasive Carcinoma (TCGA-BRCA) cohort (https://www.cancer.gov/tcga)[13]. Pathway enrichment analysis was performed using the Kyoto Encyclopedia of Genes and Genomes (KEGG) database (https://www.kegg.jp/kegg/pathway)[14]. Ligand-receptor interaction analysis was conducted using CellPhoneDB v5.0 (https://www.cellphonedb.org)[15].

Analysis of scRNA-seq data

scRNA-seq data was analyzed using the Seurat package (version 5.0.3) in R software (version 4.2.2). We first performed batch integration using the FindIntegrationAnchors and IntegrateData functions, selecting the top 30 principal components (dims = 1:30). To remove batch effects, we applied the Harmony tool for data correction [16]. We selected the top 21 Harmony features for cell clustering with the FindClusters function at a resolution of 0.5. For both myeloid and T cell

subpopulations, clustering was performed after dimensionality reduction and batch correction. Briefly, after quality control and normalization, the top variable features were identified for each subset. Batch effects were corrected using Harmony. For myeloid subpopulations, the first 12 Harmony components were used for clustering with the FindClusters function (resolution = 0.5), whereas for T cell subpopulations, the first 23 Harmony components were used (resolution = 0.5). Cluster identities were visualized using Uniform Manifold Approximation and Projection (UMAP) plots generated from the respective Harmony embeddings. Cell-type proportion differences between groups were analyzed using the *t*-test, with a P-value < 0.05 considered statistically significant. In addition, KEGG enrichment analyses were performed for each subtype feature gene using the R package clusterProfiler (v4.6.2) [17].

Pseudotime trajectory inference based on Monocle 2

We performed pseudotime trajectory analysis of the cells using the R package Monocle 2. The dpFeature function was used for unsupervised cell ordering and for selecting ordering genes. Subsequently, the cells were arranged along the trajectory through dimensionality reduction using the DDRTree algorithm.

M1/M2 signature score analysis

M1/M2 polarization scoring was performed using the singscore algorithm for single-sample gene set scoring. The polarization score for each cell was calculated based on literature-reported M1-type (IL1B, CCL2, CCL3, CCL4, TNF, CXCL2, CXCL9, CXCL10, and SOCS3) and M2-type (CD163, MRC1, MSR1, CCL13, CCL18, IL10, FOLR2, STAB1, CD163L1, SEPP1, F13A1, MERTK, AXL, CCL22, IL1RN, GPNMB, and CHI3L1) signature genes [18]. For inter-group comparisons, the Wilcoxon rank-sum test was used according to the experimental design. Statistical significance was set at adjusted $P < 0.05$.

T cell cytotoxicity/exhaustion status assessment

Cytotoxicity (GZMA, GZMB, GZMH, GZMK, GZMM, GNLY, PRF1, FASLG, IFNG, TNF, IL2R, and IL2) and exhaustion (CXCL13, HAVCR2, PDCD1, TIGIT, LAG3, CTLA4, LAYN, RBPJ, VCAM1, GZMB, TOX, and MYO7A) gene signatures were defined based on previous studies [19, 20]. Cytotoxicity and exhaustion scores for

each T cell were calculated using the singscore algorithm. Differences between groups were analyzed using the Wilcoxon rank-sum test.

Survival analysis

Survival analysis was performed using data from the TCGA-BRCA cohort to evaluate the prognostic value of Mac-SPP1 cell subtype expression. RNA-seq FPKM values were first log-transformed using the formula log2(FPKM + 1) to approximate a normal distribution. Subsequently, the optimal cut-off point for dichotomizing patients into high- and low-expression groups was determined using the maximally selected rank statistics method implemented in the R package maxstat (version 0.7.25). To ensure clinical relevance, this procedure was constrained by setting the minimum group size to include at least 25% and at most 75% of the patients. Based on this empirically determined cut-off, patients were stratified into two groups. The Kaplan-Meier survival curves for these groups were generated with the survfit function from the R survival package, and the statistical significance of differences in survival outcomes was assessed using the log-rank test. Statistical significance was set at $P < 0.05$t.

Transcription factor (TF) analysis

PySCENIC is a Python implementation of the SCENIC (Single Cell Regulatory Network Inference and Clustering) workflow, which reconstructs transcriptional regulatory networks, identifies key TFs, and characterizes cell identities from scRNA-seq data [21, 22]. We randomly selected 500 cells per group and performed TF analysis on different subpopulations using pySCENIC (v0.12.1).

Metabolic activity analysis

To assess the intrinsic metabolic state of each identified cell subtype, we performed single-cell metabolic enrichment analysis using the singscore algorithm. KEGG metabolic pathway gene sets were used as reference signatures. Enrichment scores were calculated for each cell individually, and the average score per subtype or per sample group was calculated to evaluate metabolic rewiring across biological conditions.

Cell-cell communication analysis

To decipher the potential communication between the ligands (Mac-SPP1

macrophage subset) and receptors (CD4-S100A9 or CD8-GZMK T cell subsets), we performed a ligand-receptor interaction analysis using the cellphoneDB python package and selected significant interactions with a $P < 0.05$ [23].

Results

Tumor microenvironment in breast cancer bone metastasis characterized by single-cell transcriptomic sequencing

We employed scRNA-seq to systematically analyze the cellular landscape of normal breast tissues (Normal), primary breast cancer tissues (Primary), and bone metastases of breast cancer tissues (Metastatic) to elucidate the dynamic evolution of the tumor microenvironment during cancer progression and metastasis. Following strict quality control and doublet removal, 141056 cells were retained for subsequent analyses. Integration and unsupervised clustering analysis was performed for all samples. As shown in Fig. 1A, the UMAP plot evidently shows 11 cell populations, namely T cells, fibroblasts, epithelial, myeloid cells, perivascular-like, endothelial, mast, B cells, HSPA6, cycling, and plasma. Subsequently, we analyzed the distribution of cell populations across different groups. The results revealed that compared with the Normal and Primary groups, the Metastatic group exhibited significant changes (Fig. 1B). The marker genes of different cell populations are shown in Fig. 1C. The bar plots in Fig. 1D and 1E illustrate the proportional distribution of various cell types across different groups. Some cells, such as Myeloid cells, T cells and fibroblasts, exhibited notable differences. Further statistical analysis revealed a significant increase in the proportion of Myeloid cells and T cells in the Primary groups compared with the Normal group (Fig. 1F), and a significant increase in the proportion of B cells, cycling, plasma and T cells in the Metastatic groups compared with the Normal group (Fig. 1G). In addition, the proportion of myeloid cells was significantly higher in the Metastatic group than in the Normal and Primary groups (Fig. 1H). These findings suggest that the T cells and myeloid cells play a critical role in breast cancer bone metastasis.

Characteristics and functional states of myeloid cells in the breast cancer bone

metastatic microenvironment

A total of 14216 myeloid cells were identified in all samples. Nine cell subpopulations were clustered and annotated based on marker genes, namely Mono-S100A8, Mac-SPP1, Mac-CXCL3, Mac-APOE, Mono-FCGR3A, Mono-GPX1, cDC, DC-LAMP3, and Cycling Myeloid (Fig. 2A and 2B). The marker gene expression patterns of these nine cell myeloid subpopulations are shown in a heatmap (Fig. 2C). Further analysis revealed that compared with the Normal and Primary groups, the Metastatic group exhibited a significant decrease in the proportions of Mac-APOE and Mac-CXCL3 cell subpopulations, while the proportion of Mac-SPP1 subpopulation was significantly expanded (Fig. 2D and 2E). To infer the macrophage differentiation course, we used Monocle 2 to perform trajectory analysis of these three cell subpopulations. As shown in Fig. 2F, the Mac-SPP1 subpopulation represents a terminal status with the highest pseudotime score, originating from precursor states such as Mac-APCE or Mac-CXCL3. To investigate the functional properties of key macrophage subpopulations, we assessed their M1 and M2 polarization gene signatures. The Mac-SPP1 subpopulation exhibited a typical M2-like phenotype (Fig. 2G). Correspondingly, the overall macrophage population in metastases also showed a significant bias towards the M2 state (Fig. 2H). KEGG pathway enrichment analysis revealed that differentially expressed genes (DEGs) in macrophages from the Primary and Metastatic groups were primarily enriched in pathways such as osteoclast differentiation (Fig. 2I).

Mac-SPP1 subpopulation promotes breast cancer bone metastasis

The clinical implications of the Mac-SPP1 subtypes were verified by overall survival (OS). In the Kaplan-Meier survival curves, the group with low-expression scores was significantly associated with good OS (P = 4.9e-05, log-rank test, Fig. 3A). To investigate the underlying regulatory mechanisms, we analyzed TF activity across different macrophage subpopulations. Highly active TFs in Mac-SPP1 included HOXA9, MAF, FOS, and JUND, which are associated with regulation of M2 macrophage polarization [24] (Fig. 3B). We further assessed the metabolic profiles of

these macrophages. Analysis of metabolic scores revealed that the Mac-SPP1 cell subtype exhibited the highest metabolic activity (Fig. 3C) and that the Metastatic group also exhibited elevated metabolic activity compared with the Normal and Primary groups (Fig. 3D). These findings suggest that the Mac-SPP1 macrophage subtype is associated with the progression of breast cancer bone metastasis.

Landscape, functional exhaustion, and transcriptional regulation of CD4+ T cells in bone metastasis of breast cancer

After pooling T cells by identity, clustering analysis was performed to generate a UMAP that illustrates the intercellular phenotypic heterogeneity of each cell subpopulation (Fig. 4A, 4B). Nine subclusters were identified among T cells in different groups: CD8-IL7R, CD4-LEF1, CD8-GZMK, T-CTLA4-CXCL13-n, CD8-GNLY, T-CTLA4-CXCL13-P, CD4-IKZF2, CD4-S100A9, and CD8-AFF3. The proportions of each cell type in all groups are shown in Fig. 4C, and their marker genes are displayed in Fig. 4D. Statistical analysis revealed that compared with the Primary group, the Metastatic group had significantly increased proportions of CD4-IKZF2, CD4-LEF1, CD4-S100A9, CD8-AFF3, CD8-GNLY, and CD8-GZMK (Fig. 4E). Therefore, we first focused on the three CD4+ T cell subpopulations for further investigation. The CD4-S100A9 subpopulation exhibited higher cytotoxicity and exhaustion scores (Fig. 4F). Specifically, the Metastatic group showed a significantly higher cytotoxicity score compared with the Primary group and a significantly higher exhaustion score compared with the Normal group (Fig. 4G).

We conducted pseudotime analysis on CD4+ T cell subpopulations and identified three distinct cell states and a primary continuous trajectory (Fig. 4H). Pseudotime analysis identified the CD4-S100A9 cells as the starting point of the differentiation process and the CD4-LEF1 cells as the terminal endpoint. The CD4-IKZF2 subpopulation was positioned at the intermediate stage of pseudotime, suggesting that this cluster represents a transitional or regulatory state during T cell differentiation.

CD4-S100A9 subpopulation promotes breast cancer bone metastasis

TF activity analysis revealed that the CD4-S100A9 subpopulation exhibited high activity of TFs such as YY1, CEBPD, SPI1, NFE2, JDP2, FLI1, FOSB, TFEC, MIOS, NFE2L2, FOS, TCF12, ELF1, ETV6, JUN, BACH1, and TFDP1, indicating its identity as an activated effector $CD4^+$ T cell within a highly cytotoxicity and exhaustion stressed microenvironment (Fig. 5A). KEGG analysis of the DEG profiles in $CD4^+$ T cells of the Primary and Metastatic groups revealed strong associations with pathways such as the T cell receptor signaling pathway (Fig. 5B). We then evaluated the metabolic characteristics of these $CD4^+$ T cells. The CD4-S100A9 subtype exhibited the highest metabolic activity (Fig. 5C). Moreover, compared with the Normal and Primary groups, the Metastatic group showed a marked increase in metabolic activity (Fig. 5D). These results implicate the CD4-S100A9 T cell subtype in the advancement of breast cancer bone metastasis.

Functional dynamics and developmental trajectory of $CD8^+$ T cells in the tumor microenvironment

We evaluated the levels of cytotoxicity and exhaustion of four $CD8^+$ T cell subpopulations (CD8-AFF3, CD8-GNLY, CD8-GZMK, and CD8-IL7R), implying that CD8-AFF3, CD8-GNLY and CD8-GZMK had high cytotoxicity and exhaustion scores (Fig. 6A). Cytotoxic and exhausted $CD8^+$ T cells tended to exhibit increased proportions in the Metastatic group (Fig. 6B). To further explore the dynamic transitional process of $CD8^+$ T cells, we constructed a pseudotime map of $CD8^+$ T cell state trajectory. As shown in Fig. 6C, the trajectory was started with central memory T cells (CD8-IL7R), with an effector memory $CD8^+$ T cell (CD8-GZMK) as the transitional state, and terminally reached a final differentiate state of CD8-GNLY, while another subset adopted an exhausted state (CD8-AFF3).

Mac-SPP1 interacts with CD4-S100A9 and CD8-GMZK

TF activity analysis revealed that ETV1 is highly expressed in CD8-GMZK cells (Fig. 7A). KEGG pathway enrichment results indicate that DEGs between the Metastatic and Primary groups are primarily associated with ribosome, T cell receptor

signaling pathway, and PD-L1 expression and PD-1 checkpoint pathway in cancer signaling pathways (Fig. 7B). The metabolic characteristics of these $CD8^+$ T cells were further evaluated. As shown in Fig. 7C, the CD8-GMZK subtype exhibited the higher metabolic activity. Interestingly, the Metastatic group exhibited significantly increased metabolic activity compared with the Normal and Primary groups (Fig. 7D). These findings indicate that the CD8-GMZK T cell subtype may be involved in breast cancer bone metastasis.

Cell-cell communication analysis revealed that the pro-metastatic Mac-SPP1 macrophage subpopulation could establish functional interactions with distinct T cell subsets via specific ligand-receptor pairs (Fig. 7E-F). The interactions between Mac-SPP1 and CD4-S100A9/CD8-GZMK T cells were predominantly mediated by SPP1-related pathways (e.g., SPP1-a4b1 and SPP1-CD44), as well as immunomodulatory molecular pairs such as CD74-MIF and CD74-COPA.

Discussion

This study provides a comprehensive single-cell atlas of the breast cancer bone metastatic microenvironment, revealing key immune cell subpopulations and their interactions that likely drive metastatic progression. We show that bone metastases exhibit a significant expansion of both myeloid and T cells, with specific subsets exhibiting functional and metabolic reprogramming conducive to tumor growth and immune evasion.

We identified the Mac-$SPP1^+$ macrophage subset as a metastasis-enriched, M2-polarized, and metabolically hyperactive population, consistent with previous reports on $SPP1^+$ TAMs in other cancers [25]. Previous studies have demonstrated that $SPP1^+$ macrophages can regulate resistance to neoadjuvant chemotherapy and immunotherapy in esophageal squamous cell carcinoma [26] and promote the development and progression of head and neck squamous cell carcinoma via TNF-α and IL-1β secretion [27]. In colorectal cancer, $SPP1^+$ macrophages interact with FAP^+ fibroblasts to jointly promote tumor growth [28]. They also contribute to an immunosuppressive microenvironment through interactions with cancer-associated

fibroblasts, thereby facilitating colorectal cancer liver metastasis [29]. We also found that high Mac-SPP1^{+} macrophage abundance correlated with poor survival, underscoring its potential clinical relevance. The high activity of TFs such as HOXA9 and MAF suggests a regulatory network that promotes an immunosuppressive, pro-tumorigenic phenotype. Furthermore, the increased metabolic activity in Mac-SPP1^{+} cells and the overall metastatic niche implies a nutrient-demanding microenvironment that may support tumor survival and growth.

T cells represent a major immune cell population that plays a crucial role in improving clinical outcomes in various cancers, including breast and liver cancers [30, 31]. Among T cells, we identified the CD4-S100A9^{+} subpopulation as a critical player. This subset exhibited a unique transcriptional profile indicative of an activated yet exhausted effector state, as evidenced by high cytotoxicity/exhaustion scores and pronounced metabolic activity. Its positioning at the start of the pseudotime trajectory suggests it represents an early, stress-responsive CD4^{+} T cell state within the metastatic niche. CD8+ T cells, which are key members of the adaptive immune system, also play a definitive role in tumors [32]. In the present study, the CD8-GZMK^{+} T cells showed features of exhaustion and high metabolic activity, consistent with a dysfunctional yet metabolically active state often observed in progressive tumors.

Evidence suggests that the interplay between macrophages and T cells can drive tumor progression [33]. For instance, Trehan et al. demonstrated an interaction between SPP1+ macrophages and tumor-reactive CD8+ T cells in liver cancer cells *[34]*. Another study demonstrated the interaction between SPP1+ TAMs and CD8+ exhausted T cells in metastatic gastric cancer [35]. However, the role of macrophages and T cells in breast cancer bone metastasis has not been reported. In the present study, the specific crosstalk between Mac-SPP1^{+} macrophages and T cell subsets was clarified, largely mediated by SPP1-integrin and CD74-related signaling pathways. These findings suggest a mechanism by which macrophages may directly modulate T cell function, potentially promoting exhaustion or altering differentiation, consistent with emerging evidence in glioblastoma [36].

In summary, our single-cell transcriptomic analyses of breast cancer bone

metastasis reveal a coordinated interplay between specific macrophage and T cell subsets that likely promotes an immunosuppressive, metabolically adapted microenvironment conducive to metastatic outgrowth. Targeting the Mac-SPP1–CD4-S100A9/CD8-GZMK axis may represent a promising therapeutic strategy for disrupting bone metastasis in breast cancer. Although our computational analyses provide strong associative evidence, this study has several important limitations. First, all statistical analyses were based on publicly available datasets with relatively small sample sizes: specifically, scRNA-seq data comprised 12 breast cancer bone metastasis samples, 8 primary tumors, and 4 normal samples. These limited cohort sizes may constrain statistical power and generalizability, and experimental validation is essential to corroborate our findings. For instance, functional studies using in vitro and in vivo models are required to confirm the causal roles of Mac-SPP1 and CD4-S100A9 subsets. Second, the bone metastasis and primary tumor specimens were not patient-matched (non-paired design), precluding control for inter-individual confounders and potentially obscuring true biological differences. Future work will integrate data from additional cancer types and develop a comprehensive, experimentally validated transcriptome atlas of the tumor microenvironment in breast cancer bone metastasis.

Abbreviations

scRNA-seq	single-cell RNA sequencing
LTβ	lymphotoxin-β
TF	Transcription factor
Normal	normal breast tissues
Primary	primary breast cancer tissues
Metastatic	bone metastases of breast cancer tissues

Acknowledgements

Not applicable.

Clinical trial number

Not applicable.

Author contributions

Zixue Xuan, Jun Zhang, and Kai Wang conceptualized and designed the study. Zhongxiu Wu, Yuting Zhong, Jinying Jiang and Lei Cheng conducted the bioinformatics analysis, Zixue Xuan and Yuan Zhang drafted the manuscript.

Funding

This work was supported by Key Laboratory for Cancer Prevention and treatment of Guizhou Province (QKHPT[2025]031), Key Laboratory of Clinical Pharmacology and Rational Drug Use of Bijie City (BKHPT[2025]17), Zhejiang Administration of Traditional Chinese Medicine (GZY-ZJ-KJ-23057), the Science and Technonlogy Bureau of Bijie City (BKLH[2025]71).

Data Availability Statement

The datasets used and/or analyzed during the current study are available from public repositories: scRNA-seq data were obtained from GSE266330 and GSE243526, which were downloaded from the GEO database (https://www.ncbi.nlm.nih.gov/geo/). The transcriptome and clinical data were retrieved from TCGA-BRCA cohort (https://www.cancer.gov/tcga). Pathway enrichment analysis was performed using the KEGG database (https://www.kegg.jp/kegg/pathway). Ligand-receptor interaction analysis was conducted using CellPhoneDB v5.0 (https://www.cellphonedb.org). Detailed data processing workflows are provided in the Materials and Methods section. The code used in the study is available from the corresponding author upon request.

Declarations

Ethics approval and consent to participate

Not applicable.

Consent for publication

Not applicable.

Competing interests

The authors declare that they have no competing interests.

References

1. Huang G, Yu Y, Su H, Gan H, Chu L: **Integrating RNA-seq and scRNA-seq to explore the prognostic features and immune landscape of exosome-related genes in breast cancer metastasis.** *Ann Med* 2025, **57:**2447917.
2. Zarrer J, Haider MT, Smit DJ, Taipaleenmäki H: **Pathological Crosstalk between Metastatic Breast Cancer Cells and the Bone Microenvironment.** *Biomolecules* 2020, **10**.
3. Magno E, Bussard KM: **A Representative Clinical Course of Progression, with Molecular Insights, of Hormone Receptor-Positive, HER2-Negative Bone Metastatic Breast Cancer.** *Int J Mol Sci* 2024, **25**.
4. Yip RKH, Rimes JS, Capaldo BD, Vaillant F, Mouchemore KA, Pal B, Chen Y, Surgenor E, Murphy AJ, Anderson RL, et al: **Mammary tumour cells remodel the bone marrow vascular microenvironment to support metastasis.** *Nat Commun* 2021, **12:**6920.
5. Gong H, Li Y, Yang W, Xie Z, Hu J, Li P, Xu R, Li Y, Tao T, Li R, et al: **PRODH2-Mediated Metabolism in the Bone Microenvironment Promotes Breast Cancer Metastasis.** *Cancer Res* 2025, **85:**4198-4211.
6. Zhang M, Tang C, Li S, Jiang X, Li B, Chen Y, Zheng Q, Tang Y, Zhu X, Huang L, et al: **NSUN2-mediated m(5)C modification of KDM6B mRNA enhances osteoclast differentiation and promotes breast cancer bone metastasis.** *Cancer Lett* 2025, **631:**217939.
7. Xu L, Yu Q, Peihang X, Li K, Wang B, Shao Y, Cheng M, Huang W, Yao Q, Feng X, et al: **YTHDF3 promotes breast cancer osteolytic bone metastasis by enhancing the translation of ZEB1 and SMAD5.** *Oncogenesis* 2025, **14:**41.
8. Li C, Liu D, Yang S, Hua K: **Integrated single-cell transcriptome analysis of the tumor ecosystems underlying cervical cancer metastasis.** *Front Immunol* 2022, **13:**966291.

9. Wu Q, Tian P, He D, Jia Z, He Y, Luo W, Lv X, Wang Y, Zhang P, Liang Y, et al: **SCUBE2 mediates bone metastasis of luminal breast cancer by modulating immune-suppressive osteoblastic niches.** *Cell Res* 2023, **33:**464-478.
10. Wang X, Zhang T, Zheng B, Lu Y, Liang Y, Xu G, Zhao L, Tao Y, Song Q, You H, et al: **Lymphotoxin-β promotes breast cancer bone metastasis colonization and osteolytic outgrowth.** *Nat Cell Biol* 2024, **26:**1597-1612.
11. Regner MJ, Garcia-Recio S, Thennavan A, Wisniewska K, Mendez-Giraldez R, Felsheim B, Spanheimer PM, Parker JS, Perou CM, Franco HL: **Defining the regulatory logic of breast cancer using single-cell epigenetic and transcriptome profiling.** *Cell Genom* 2025, **5:**100765.
12. Liu F, Ding Y, Xu Z, Hao X, Pan T, Miles G, Wang S, Wu YH, Liu J, Bado IL, et al: **Single-cell profiling of bone metastasis ecosystems from multiple cancer types reveals convergent and divergent mechanisms of bone colonization.** *Cell Genom* 2025, **5:**100888.
13. **Comprehensive molecular portraits of human breast tumours.** *Nature* 2012, **490:**61-70.
14. Kanehisa M, Furumichi M, Sato Y, Ishiguro-Watanabe M, Tanabe M: **KEGG: integrating viruses and cellular organisms.** *Nucleic Acids Res* 2021, **49:**D545-d551.
15. Efremova M, Vento-Tormo M, Teichmann SA, Vento-Tormo R: **CellPhoneDB: inferring cell-cell communication from combined expression of multi-subunit ligand-receptor complexes.** *Nat Protoc* 2020, **15:**1484-1506.
16. Korsunsky I, Millard N, Fan J, Slowikowski K, Zhang F, Wei K, Baglaenko Y, Brenner M, Loh PR, Raychaudhuri S: **Fast, sensitive and accurate integration of single-cell data with Harmony.** *Nat Methods* 2019, **16:**1289-1296.
17. Xuan Z, Wang K, Zhu Q, Sun T, Jiang J, Wu Z, Zheng S, Zhao H: **Neoadjuvant PD-1 blockade induces the autophagy of immune cells: a new target for synergistic therapy of recurrent glioblastoma.** *Biochem Biophys Rep* 2025, **43:**102119.

18. Qian J, Olbrecht S, Boeckx B, Vos H, Laoui D, Etlioglu E, Wauters E, Pomella V, Verbandt S, Busschaert P, et al: **A pan-cancer blueprint of the heterogeneous tumor microenvironment revealed by single-cell profiling.** *Cell Res* 2020, **30:**745-762.

19. Wu SZ, Al-Eryani G, Roden DL, Junankar S, Harvey K, Andersson A, Thennavan A, Wang C, Torpy JR, Bartonicek N, et al: **A single-cell and spatially resolved atlas of human breast cancers.** *Nat Genet* 2021, **53:**1334-1347.

20. Zhang Y, Chen H, Mo H, Hu X, Gao R, Zhao Y, Liu B, Niu L, Sun X, Yu X, et al: **Single-cell analyses reveal key immune cell subsets associated with response to PD-L1 blockade in triple-negative breast cancer.** *Cancer Cell* 2021, **39:**1578-1593.e1578.

21. Liu K, Han H, Xiong K, Zhai S, Yang X, Yu X, Chen B, Liu M, Dong Q, Meng H, Gu Y: **Single-cell landscape of intratumoral heterogeneity and tumor microenvironment remolding in pre-nodal metastases of breast cancer.** *J Transl Med* 2024, **22:**804.

22. Wen S, Lv X, Li P, Li J, Qin D: **Analysis of cancer-associated fibroblasts in cervical cancer by single-cell RNA sequencing.** *Aging (Albany NY)* 2023, **15:**15340-15359.

23. Dinh HQ, Pan F, Wang G, Huang QF, Olingy CE, Wu ZY, Wang SH, Xu X, Xu XE, He JZ, et al: **Integrated single-cell transcriptome analysis reveals heterogeneity of esophageal squamous cell carcinoma microenvironment.** *Nat Commun* 2021, **12:**7335.

24. Ko SY, Ladanyi A, Lengyel E, Naora H: **Expression of the homeobox gene HOXA9 in ovarian cancer induces peritoneal macrophages to acquire an M2 tumor-promoting phenotype.** *Am J Pathol* 2014, **184:**271-281.

25. Wang C, Li Y, Wang L, Han Y, Gao X, Li T, Liu M, Dai L, Du R: **SPP1 represents a therapeutic target that promotes the progression of oesophageal squamous cell carcinoma by driving M2 macrophage infiltration.** *Br J Cancer* 2024, **130:**1770-1782.

26. Geng Z, Li F, Yang Z, Li B, Xu Y, Wu B, Sheng Y, Yuan P, Huang L, Qi Y: **Integrative analyses of bulk and single-cell RNA-seq reveals the correlation between SPP1(+) macrophages and resistance to neoadjuvant chemoimmunotherapy in esophageal squamous cell carcinoma.** *Cancer Immunol Immunother* 2024, **73:**257.

27. Liu C, Wu K, Li C, Zhang Z, Zhai P, Guo H, Zhang J: **SPP1+ macrophages promote head and neck squamous cell carcinoma progression by secreting TNF-α and IL-1β.** *J Exp Clin Cancer Res* 2024, **43:**332.

28. Qi J, Sun H, Zhang Y, Wang Z, Xun Z, Li Z, Ding X, Bao R, Hong L, Jia W, et al: **Single-cell and spatial analysis reveal interaction of FAP(+) fibroblasts and SPP1(+) macrophages in colorectal cancer.** *Nat Commun* 2022, **13:**1742.

29. Sathe A, Mason K, Grimes SM, Zhou Z, Lau BT, Bai X, Su A, Tan X, Lee H, Suarez CJ, et al: **Colorectal Cancer Metastases in the Liver Establish Immunosuppressive Spatial Networking between Tumor-Associated SPP1+ Macrophages and Fibroblasts.** *Clin Cancer Res* 2023, **29:**244-260.

30. Stanton SE, Disis ML: **Clinical significance of tumor-infiltrating lymphocytes in breast cancer.** *J Immunother Cancer* 2016, **4:**59.

31. Zheng C, Zheng L, Yoo JK, Guo H, Zhang Y, Guo X, Kang B, Hu R, Huang JY, Zhang Q, et al: **Landscape of Infiltrating T Cells in Liver Cancer Revealed by Single-Cell Sequencing.** *Cell* 2017, **169:**1342-1356.e1316.

32. He M, Jiang X, Miao J, Feng W, Xie T, Liao S, Qin Z, Tang H, Lin C, Li B, et al: **A new insight of immunosuppressive microenvironment in osteosarcoma lung metastasis.** *Exp Biol Med (Maywood)* 2023, **248:**1056-1073.

33. Kzhyshkowska J, Shen J, Larionova I: **Targeting of TAMs: can we be more clever than cancer cells?** *Cell Mol Immunol* 2024, **21:**1376-1409.

34. Trehan R, Huang P, Zhu XB, Wang X, Soliman M, Strepay D, Nur A, Kedei N, Arhin M, Ghabra S, et al: **SPP1 + macrophages cause exhaustion of tumor-specific T cells in liver metastases.** *Nat Commun* 2025, **16:**4242.

35. Du Y, Lin Y, Gan L, Wang S, Chen S, Li C, Hou S, Hu B, Wang B, Ye Y, Shen Z: **Potential crosstalk between SPP1 + TAMs and CD8 + exhausted T cells**

promotes an immunosuppressive environment in gastric metastatic cancer. *J Transl Med* 2024, **22:**158.

36. Ellert-Miklaszewska A, Pilanc P, Poleszak K, Roura AJ, Cyranowski S, Ghosh M, Baluszek S, Pasierbinska M, Gielniewski B, Swatler J, et al: **7aaRGD - a novel SPP1/integrin signaling-blocking peptide reverses immunosuppression and improves anti-PD-1 immunotherapy outcomes in experimental gliomas.** *J Exp Clin Cancer Res* 2025, **44:**132.

Figure captions

Figure 1. Single-cell transcriptomic analysis of Normal, Primary, and Metastatic groups. (A) UMAP visualization of single cells colored by cell type, with shading indicating clusters within each type. (B) UMAP plots of single cells from the Normal, Primary, and Metastatic groups. (C) Heatmap showing expression levels of marker genes across different cell populations. (D) Bar plots showing the proportions of cell types among total cells in different sample types. (E) Proportion of cell types in different groups. (F–H) Comparison of cell-type proportions between groups: (F) Normal vs. Primary, (G) Normal vs. Metastatic, and (H) Primary vs. Metastatic. Statistical significance was assessed using the *t*-test.

Figure 2. Transcriptional and cellular landscape of myeloid cells. (A) UMAP visualization of myeloid cell subpopulations. (B) UMAP plot showing the distribution of myeloid cells grouped by sample sites, with cells color-coded into nine clusters. (C) Heatmap showing expression levels of maker genes across different myeloid subpopulations. (D) Proportions of myeloid subpopulations in the Normal, Primary, and Metastatic groups. (E) Proportions of myeloid subpopulations in different groups. Statistical significance was assessed using the *t*-test. (F) Pseudotime trajectory of differentiation of macrophage subpopulations (Mac-APCE, Mac-CXCL3, and Mac-SPP1) inferred by Monocle. (G) Violin plot showing M1 and M2 gene signatures in Mac-SPP1, Mac-APOE, and Mac-CXCL3 cell subpopulations. (H) M1 and M2 gene signatures in the Normal, Primary, and Metastatic groups. (I) KEGG pathway enrichment analysis of DEGs in macrophages from the Primary and Metastatic groups.

Figure 3. Mac-SPP1 macrophage subpopulation is associated with poor prognosis and has the highest metabolic scores. (A) Kaplan-Meier curves showing the survival differences between the high- and low-expression groups classified by Mac-SPP1 cell subtypes. (B) Heatmap of TF activity signatures across macrophage subpopulations. (C) Metabolic scores of the three macrophage cell subtypes. (D) Metabolic scores across the Normal, Primary, and Metastatic groups.

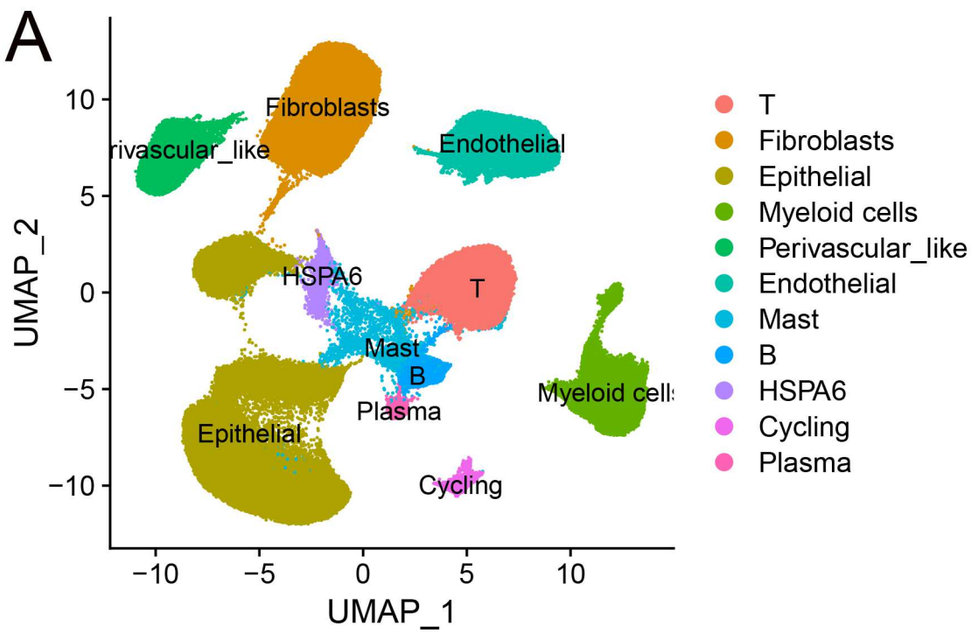
Figure 4. Transcriptional and cellular landscape of CD4+ T cells. (A, B) UMAP visualization of T cell subpopulations (A) in different groups (B). (C) Proportions of T cell subpopulations in different groups. (D) Heatmap showing expression levels of marker genes across different T cell subpopulations. (E) Statistical analysis of the proportions of CD4+ T cell subpopulations. (F, G) Cytotoxicity and exhaustion scores across $CD4^+$ T cell subpopulations (F) in different groups (G). (H) Trajectory inference reveals a potential differentiation path among $CD4^+$ T cell subpopulations.

Figure 5. $CD4^+$ T cell subpopulations undergo transcriptional, functional, and metabolic. (A, B) Heatmap of TF activity signatures across $CD4^+$ T subpopulations (A) in different groups (B). (B) KEGG pathway enrichment analysis of DEGs in $CD4^+$ T cells from the Primary and Metastatic groups. (C) Metabolic scores of the three $CD4^+$ T cell subtypes. (D) Metabolic scores across the Normal, Primary, and Metastatic groups.

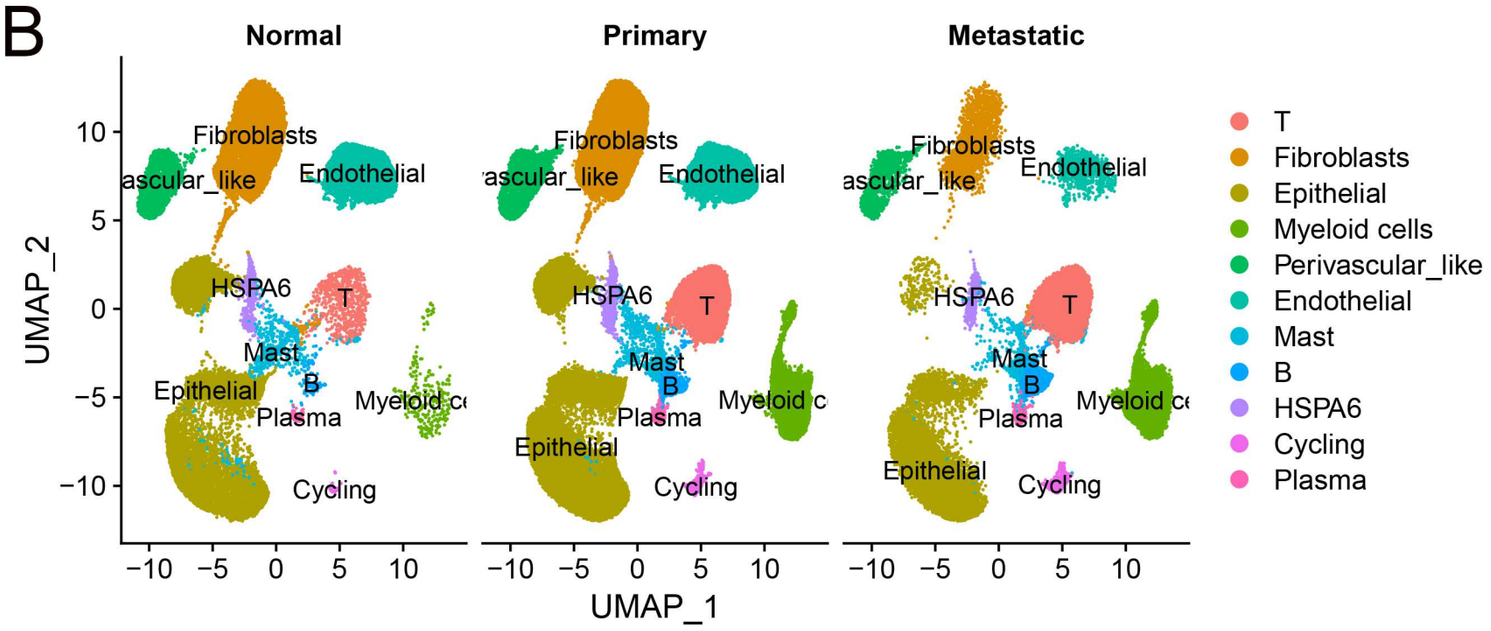
Figure 6. Cytotoxic and exhaustion phenotypes of $CD8^+$ T cells and their differentiation trajectory. (A) Cytotoxicity and exhaustion scores across $CD8^+$ T cell subpopulations and (B) their distribution in the Normal, Primary, and Metastatic groups. (C) Trajectory inference reveals a potential differentiation path among $CD8^+$ T cell subpopulations.

Figure 7. Transcriptional and cellular landscape of $CD8^+$ T cells. (A) Heatmap of TF activity signatures across $CD8^+$ T subpopulations. (B) KEGG pathway enrichment analysis of DEGs in $CD8^+$ T cells from the Primary and Metastatic groups. (C) Metabolic scores of the three $CD8^+$ cell subtypes. (D) Metabolic scores across the Normal, Primary, and Metastatic groups. (E, F) Cell-cell communication between Mac-SPP1 and CD4-S100A9 (E) and Mac-SPP1 and CD8-GZMK (F).

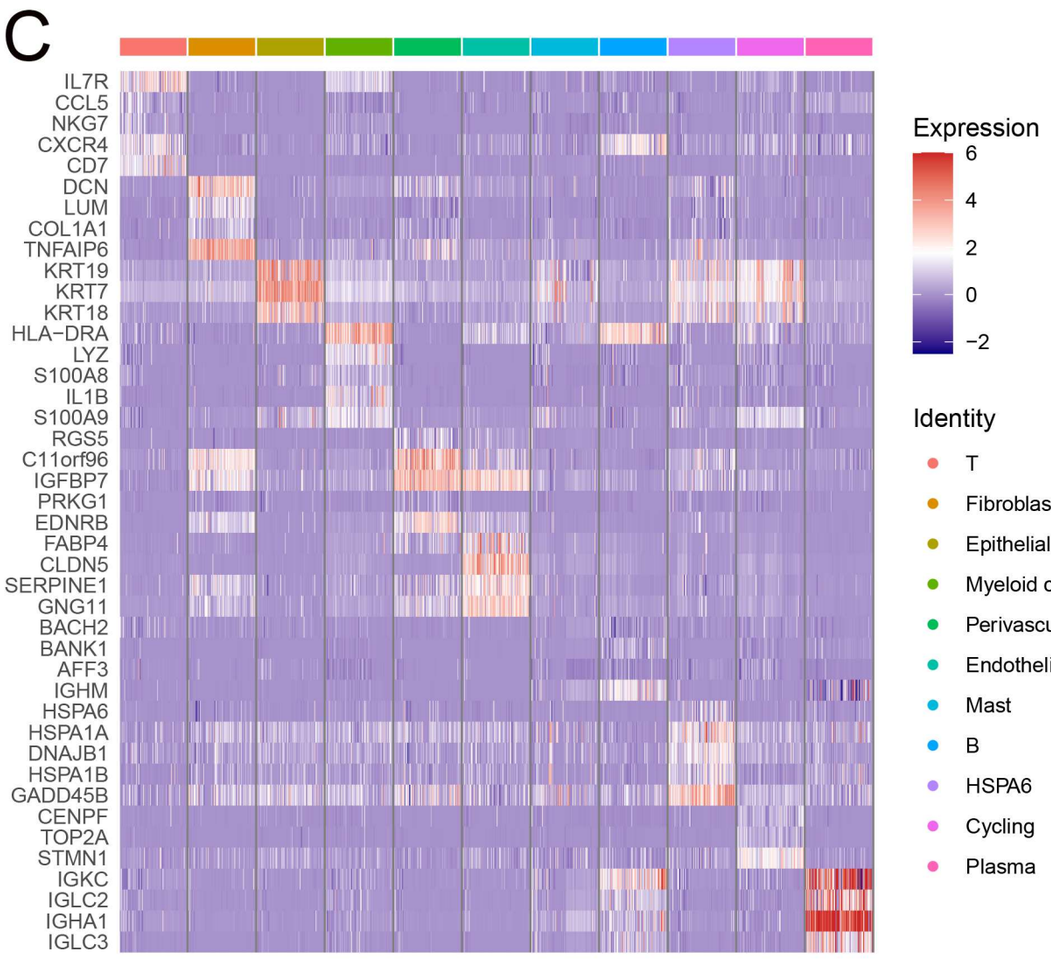
A


Fibroblasts
Endothelial
HSPA6
T
Mast
B
Plasma
Myeloid cells
Epithelial
Cycling
UMAP_1
UMAP_2
T
Fibroblasts
Epithelial
Myeloid cells
Perivascular_like
Endothelial
Mast
B
HSPA6
Cycling
Plasma

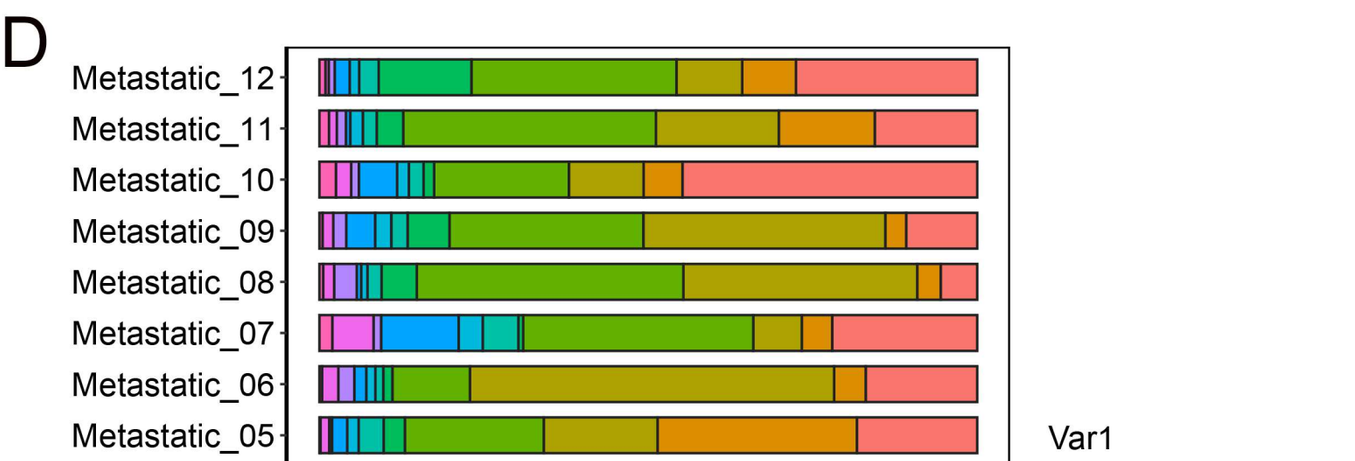
B


Normal
Primary
Metastatic
UMAP_1
UMAP_2
T
Fibroblasts
Epithelial
Myeloid cells
Perivascular_like
Endothelial
Mast
B
HSPA6
Cycling
Plasma

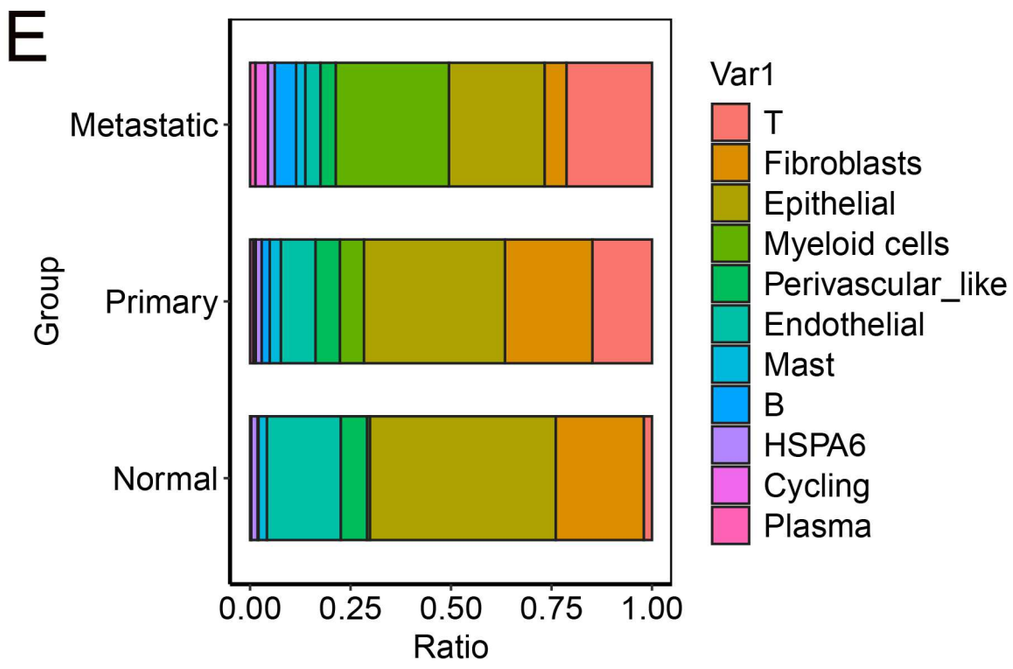
C


IL7R
CCL5
NKG7
CXCR4
CD7
DCN
LUM
COL1A1
TNFAIP6
KRT19
KRT7
KRT18
HLA-DRA
LYZ
S100A8
IL1B
S100A9
RGS5
C11orf96
IGFBP7
PRKG1
EDNRB
FABP4
CLDN5
SERPINE1
GNG11
BACH2
BANK1
AFF3
IGHM
HSPA6
HSPA1A
DNAJB1
HSPA1B
GADD45B
CENPF
TOP2A
STMN1
IGKC
IGLC2
IGHA1
IGLC3
Expression
6
4
2
0
−2
Identity
T
Fibroblasts
Epithelial
Myeloid cells
Perivascular_like
Endothelial
Mast
B
HSPA6
Cycling
Plasma

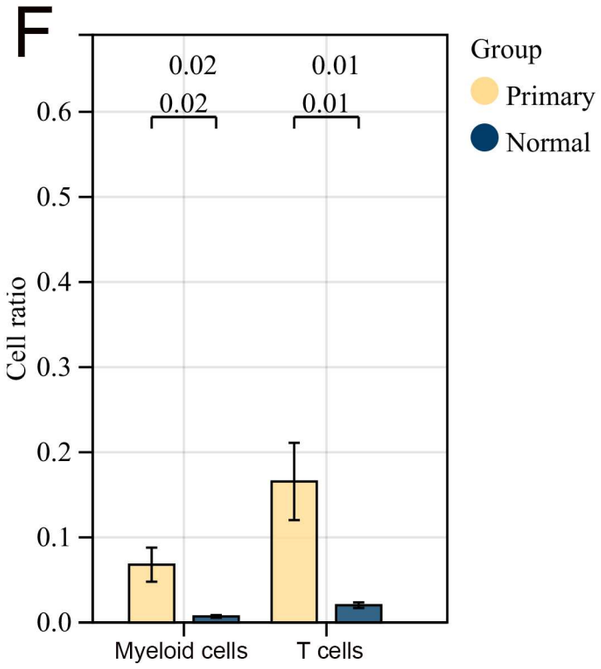
D


Metastatic_12
Metastatic_11
Metastatic_10
Metastatic_09
Metastatic_08
Metastatic_07
Metastatic_06
Metastatic_05
Metastatic_04
Metastatic_03
Metastatic_02
Metastatic_01
Primary_8
Primary_7
Primary_6
Primary_5
Primary_4
Primary_3
Primary_2
Primary_1
Normal_4
Normal_3
Normal_2
Normal_1
Sample
0.00
0.25
0.50
0.75
1.00
Ratio
Var1
T
Fibroblasts
Epithelial
Myeloid cells
Perivascular_like
Endothelial
Mast
B
HSPA6
Cycling
Plasma

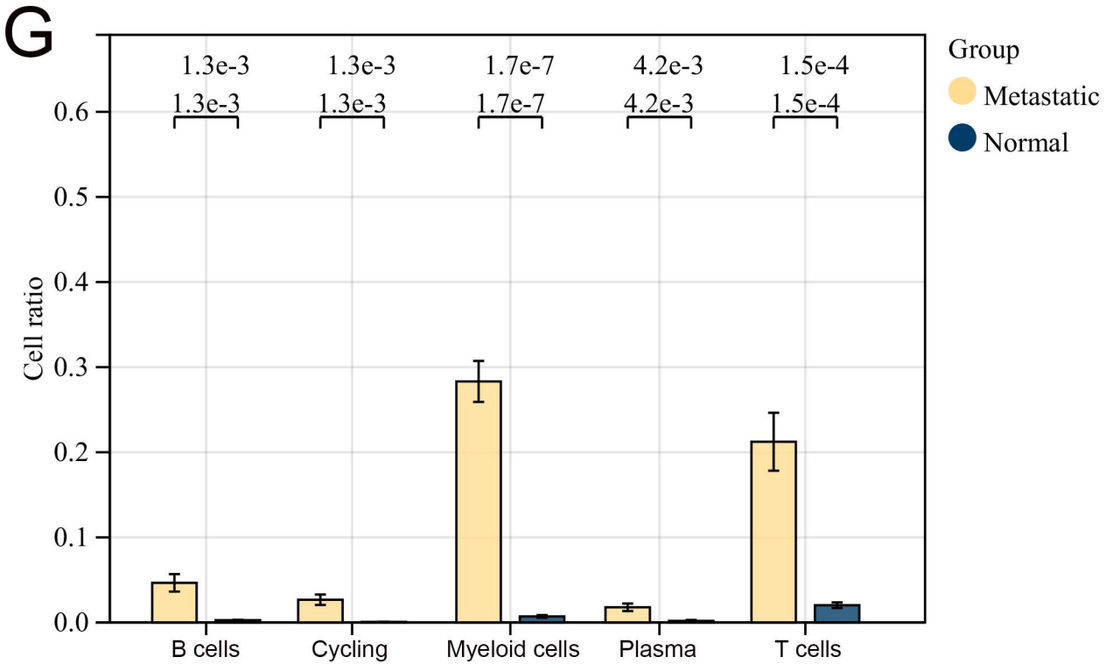
E


Metastatic
Primary
Normal
Group
0.00
0.25
0.50
0.75
1.00
Ratio
Var1
T
Fibroblasts
Epithelial
Myeloid cells
Perivascular_like
Endothelial
Mast
B
HSPA6
Cycling
Plasma

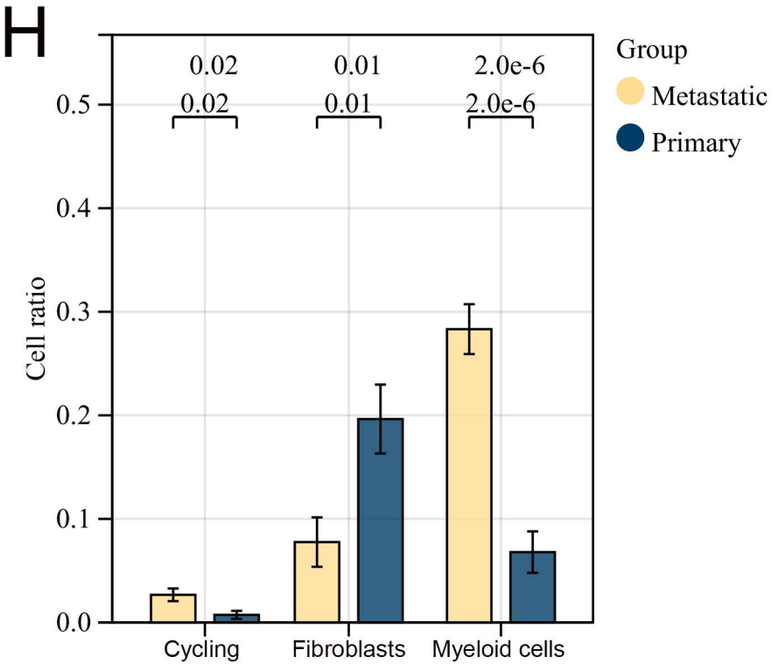
F

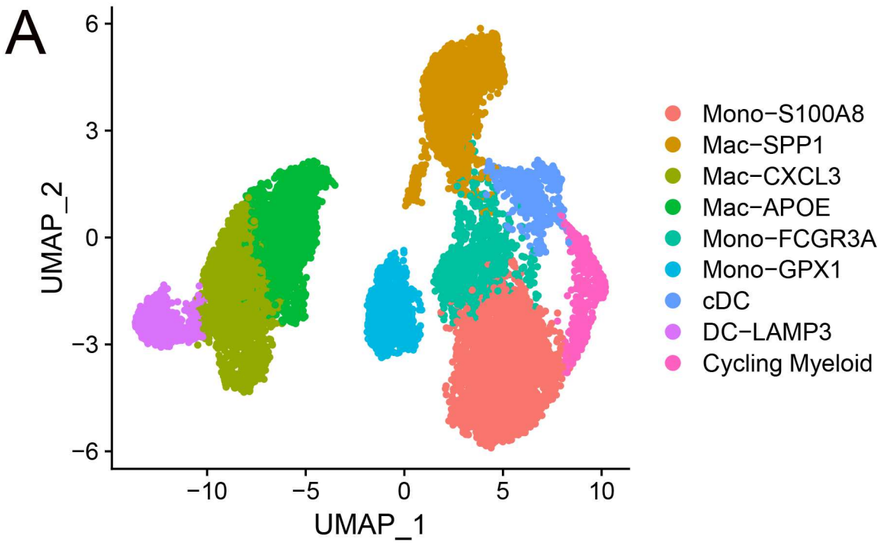

0.02
0.01
0.02
0.01
Cell ratio
0.0
0.1
0.2
0.3
0.4
0.5
0.6
Myeloid cells
T cells
Group
Primary
Normal

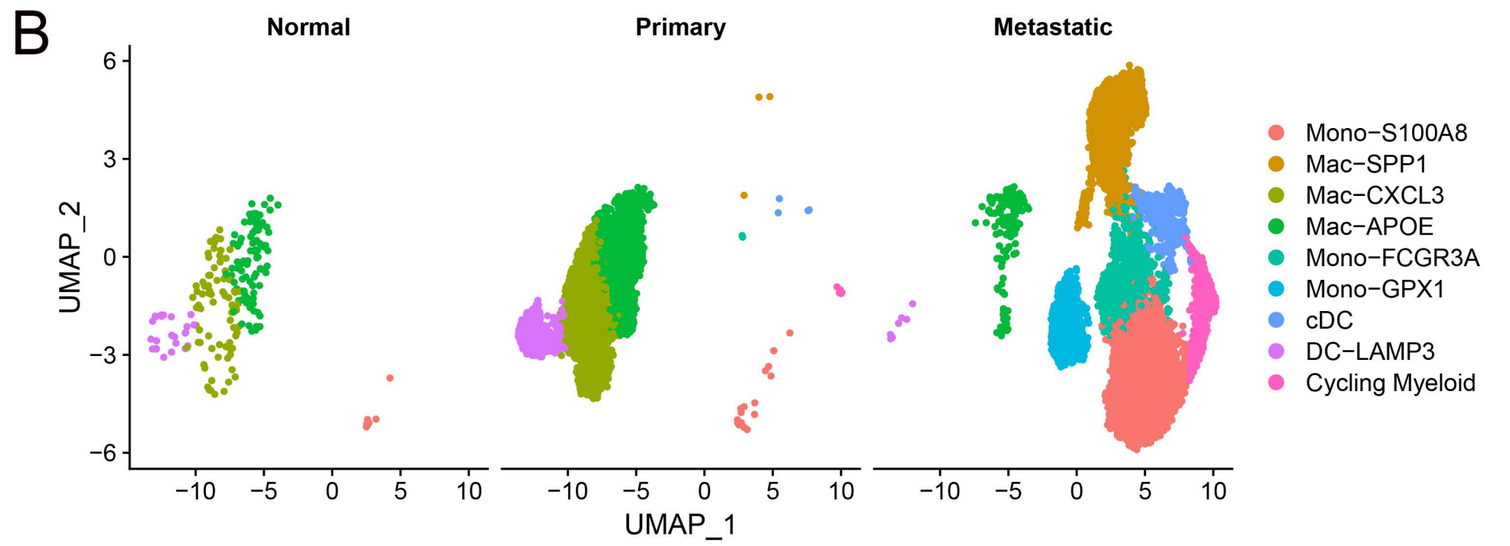
G

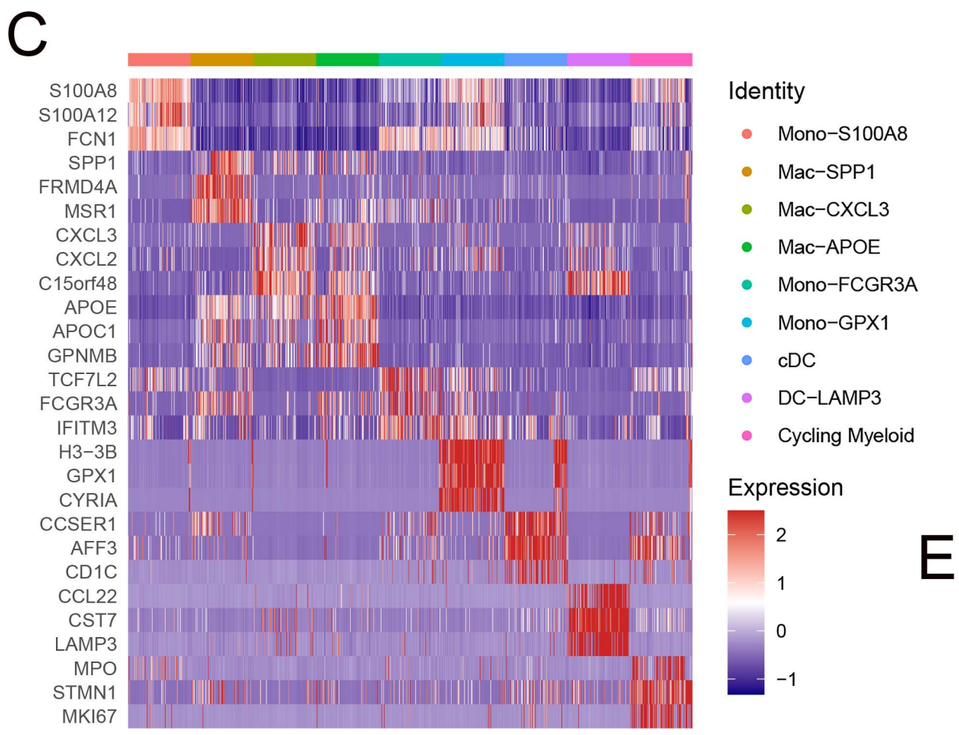

1.3e-3
1.3e-3
1.3e-3
1.3e-3
1.7e-7
1.7e-7
4.2e-3
4.2e-3
1.5e-4
1.5e-4
Cell ratio
0.0
0.1
0.2
0.3
0.4
0.5
0.6
B cells
Cycling
Myeloid cells
Plasma
T cells
Group
Metastatic
Normal

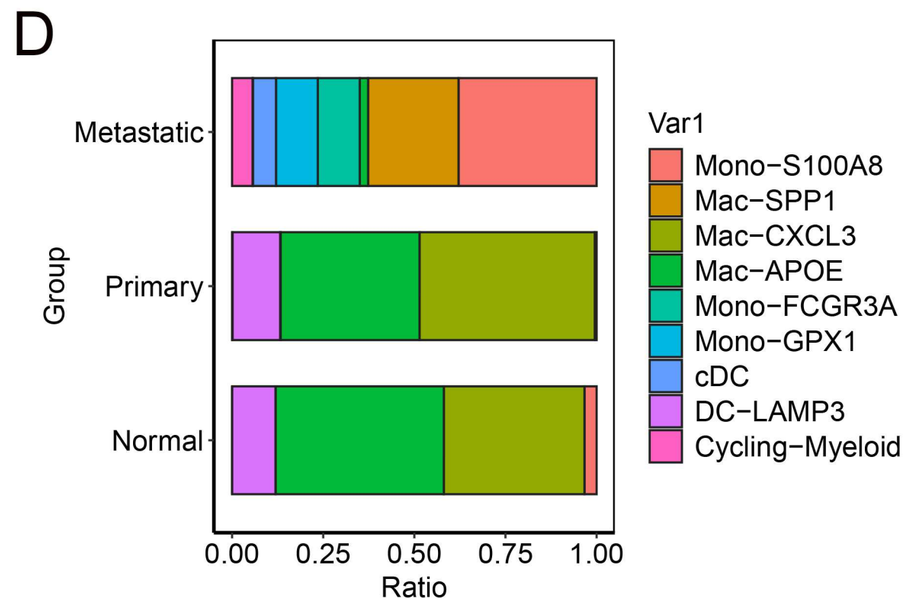
H

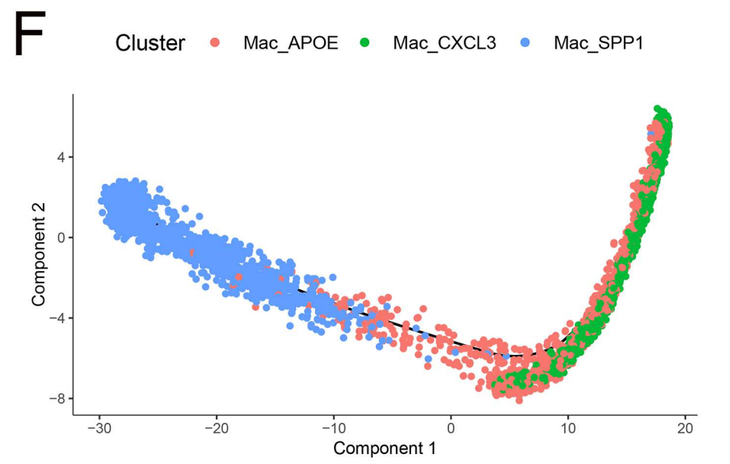

0.02
0.01
2.0e-6
0.02
0.01
2.0e-6
Cell ratio
0.0
0.1
0.2
0.3
0.4
0.5
Cycling
Fibroblasts
Myeloid cells
Group
Metastatic
Primary

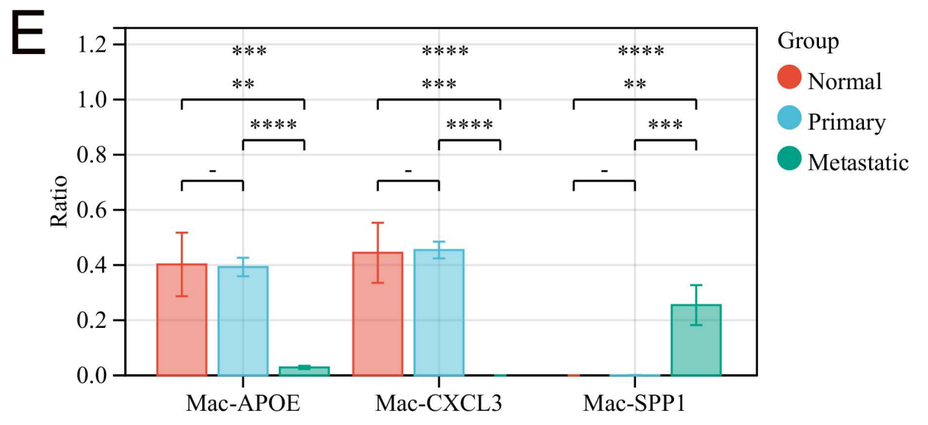

A
UMAP_2
UMAP_1
Mono−S100A8
Mac−SPP1
Mac−CXCL3
Mac−APOE
Mono−FCGR3A
Mono−GPX1
cDC
DC−LAMP3
Cycling Myeloid

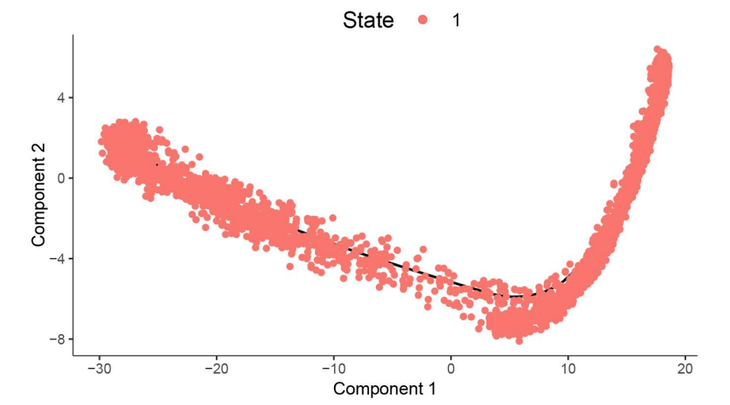

B
Normal
Primary
Metastatic
UMAP_2
UMAP_1
Mono−S100A8
Mac−SPP1
Mac−CXCL3
Mac−APOE
Mono−FCGR3A
Mono−GPX1
cDC
DC−LAMP3
Cycling Myeloid

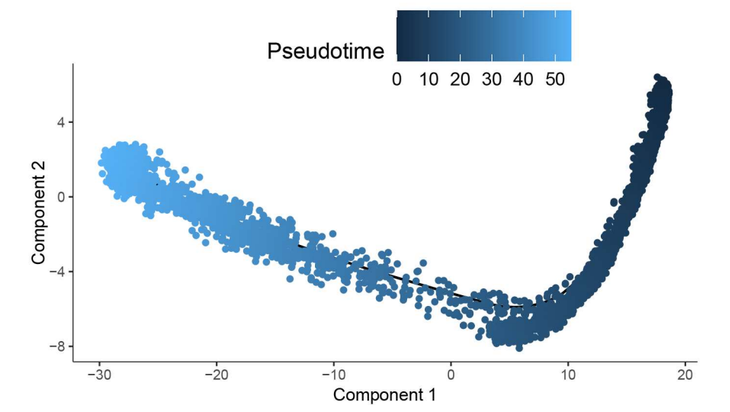

C
S100A8
S100A12
FCN1
SPP1
FRMD4A
MSR1
CXCL3
CXCL2
C15orf48
APOE
APOC1
GPNMB
TCF7L2
FCGR3A
IFITM3
H3−3B
GPX1
CYRIA
CCSER1
AFF3
CD1C
CCL22
CST7
LAMP3
MPO
STMN1
MKI67
Identity
Mono−S100A8
Mac−SPP1
Mac−CXCL3
Mac−APOE
Mono−FCGR3A
Mono−GPX1
cDC
DC−LAMP3
Cycling Myeloid
Expression

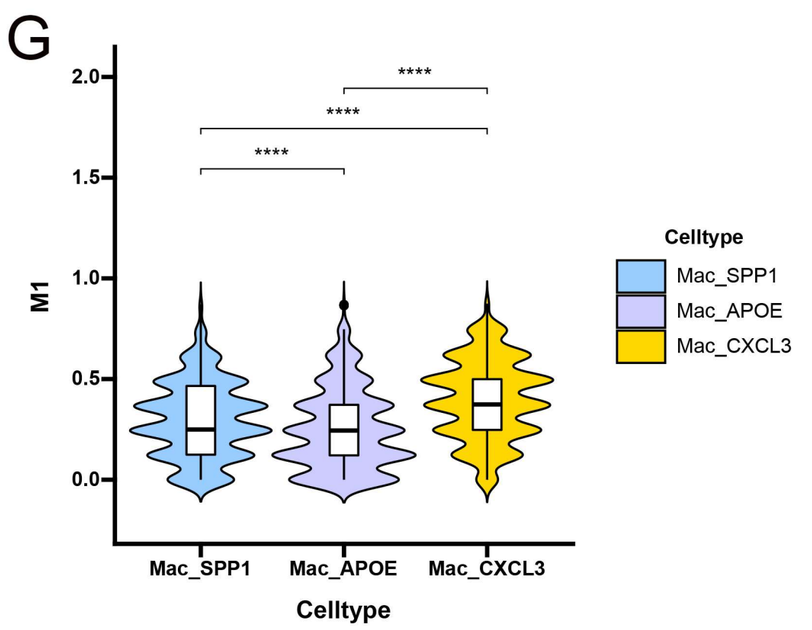

D
Metastatic
Primary
Normal
Group
Ratio
Var1
Mono−S100A8
Mac−SPP1
Mac−CXCL3
Mac−APOE
Mono−FCGR3A
Mono−GPX1
cDC
DC−LAMP3
Cycling−Myeloid

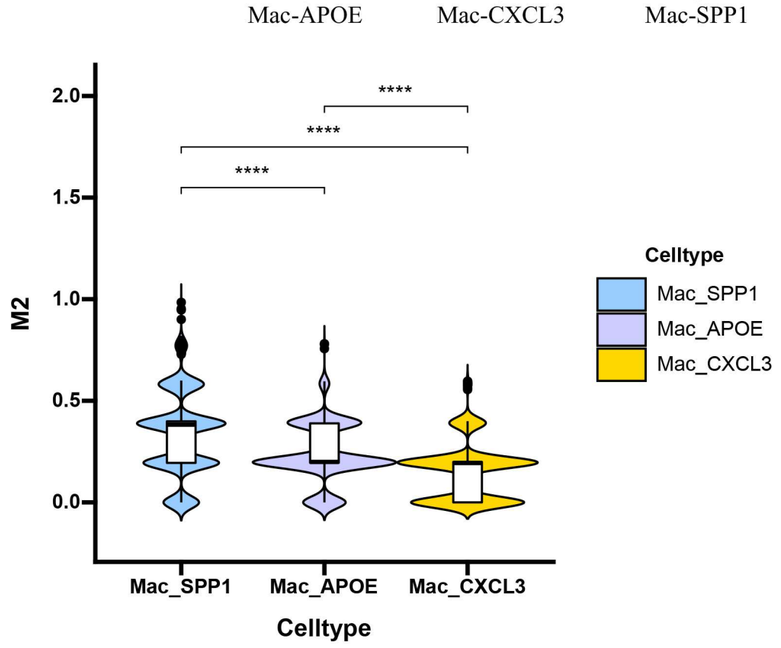

F
Cluster
Mac_APOE
Mac_CXCL3
Mac_SPP1
Component 2
Component 1

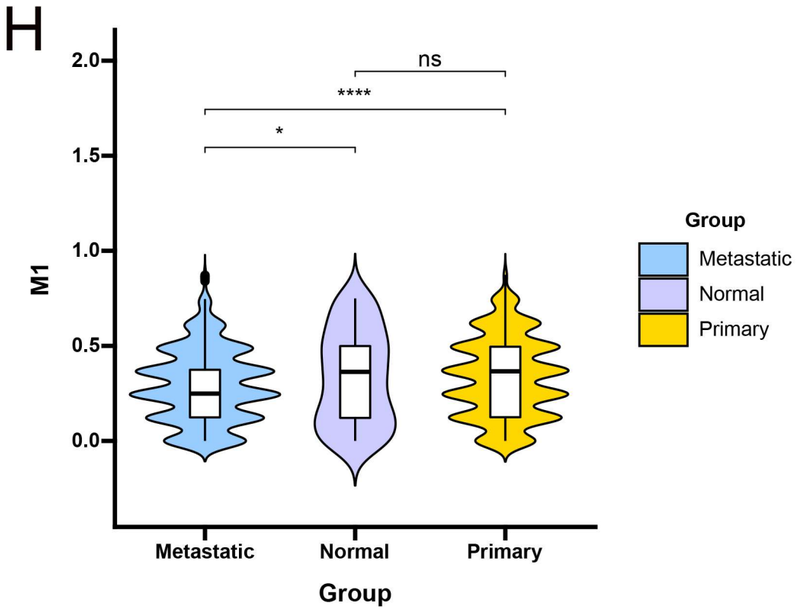

E
Ratio
Group
Normal
Primary
Metastatic
Mac-APOE
Mac-CXCL3
Mac-SPP1

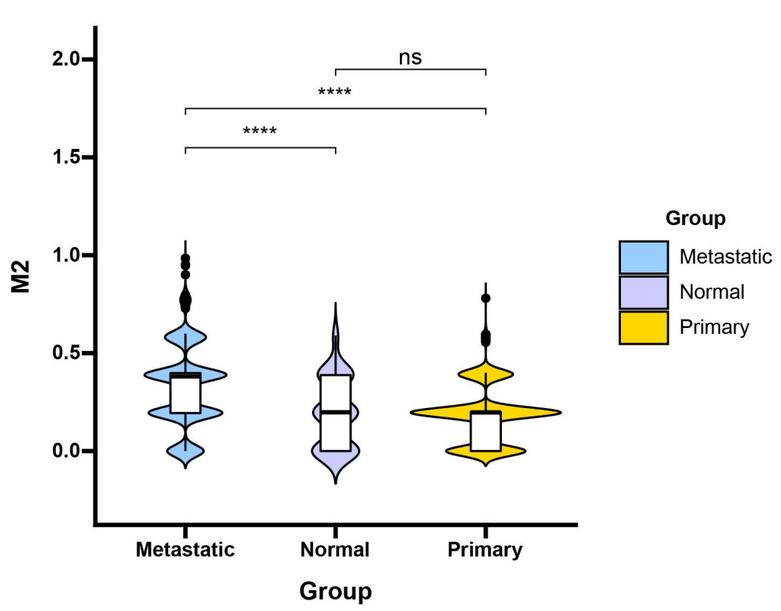

State
1
Component 2
Component 1

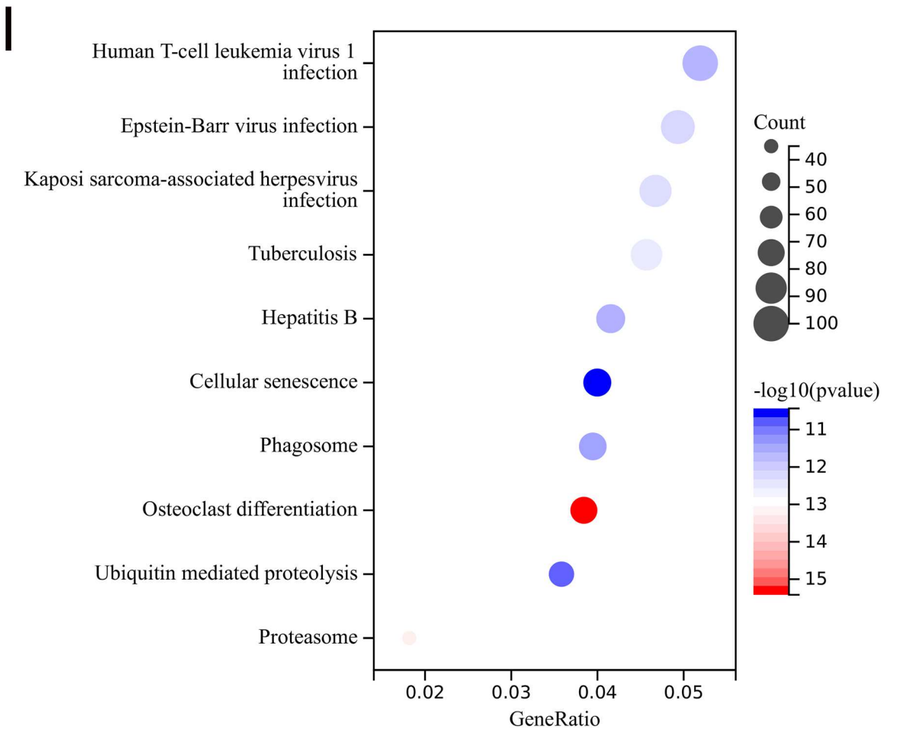

Pseudotime
0 10 20 30 40 50
Component 2
Component 1


G
M1
Celltype
Mac_SPP1
Mac_APOE
Mac_CXCL3

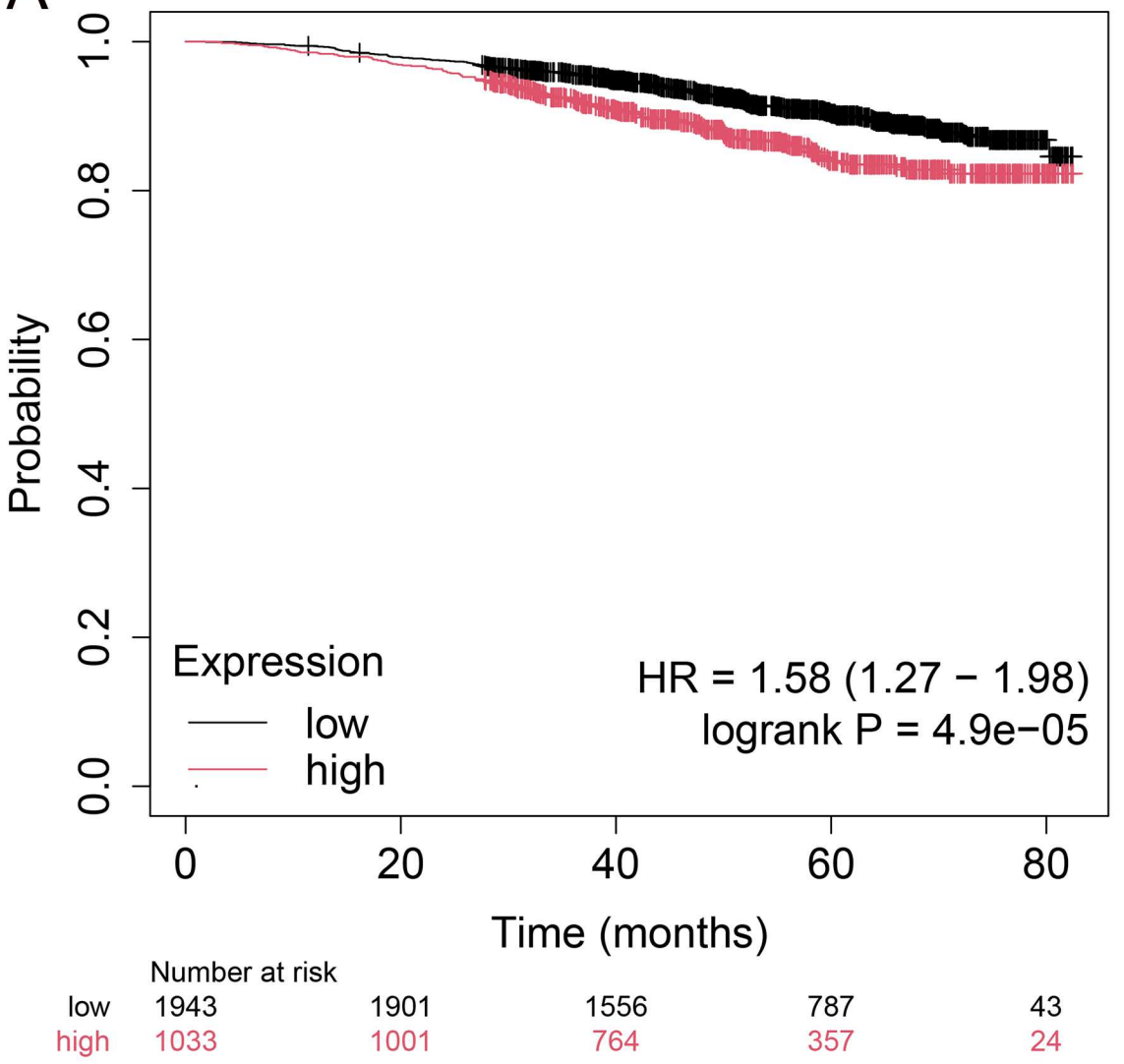

M2
Celltype
Mac_SPP1
Mac_APOE
Mac_CXCL3


H
M1
Group
Metastatic
Normal
Primary

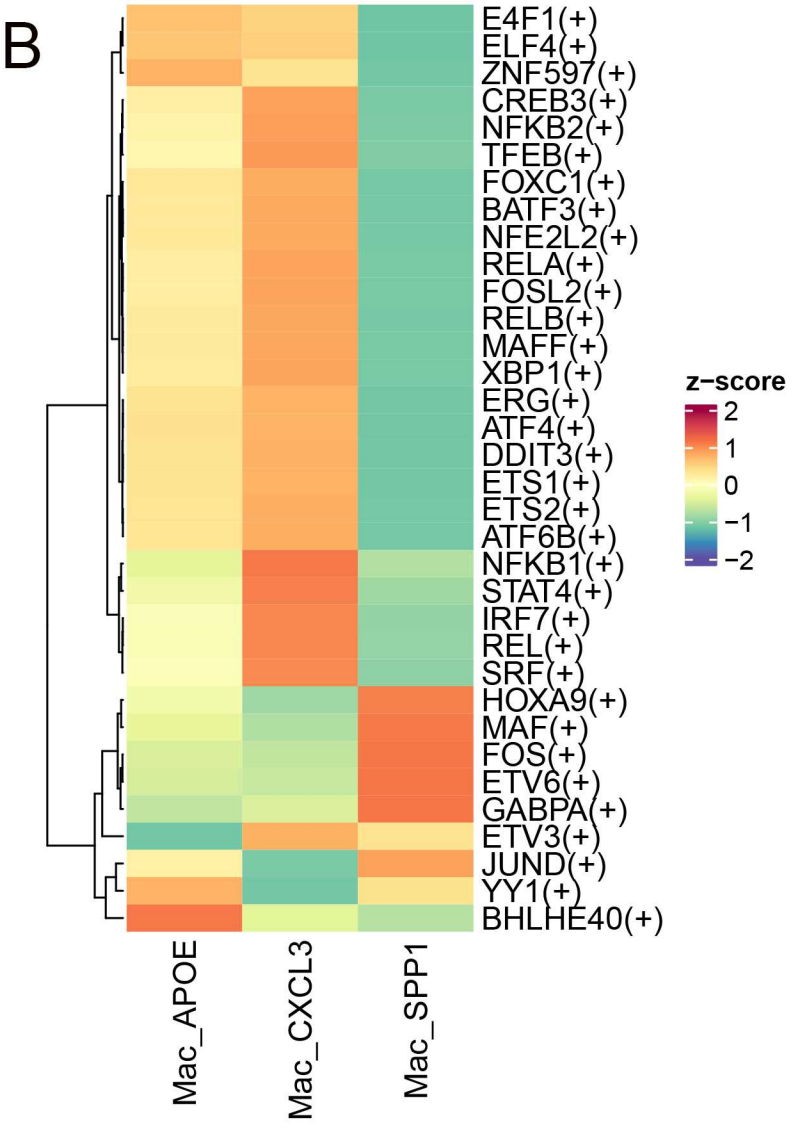

M2
Group
Metastatic
Normal
Primary


I
Human T-cell leukemia virus 1 infection
Epstein-Barr virus infection
Kaposi sarcoma-associated herpesvirus infection
Tuberculosis
Hepatitis B
Cellular senescence
Phagosome
Osteoclast differentiation
Ubiquitin mediated proteolysis
Proteasome
Count
-log10(pvalue)
GeneRatio

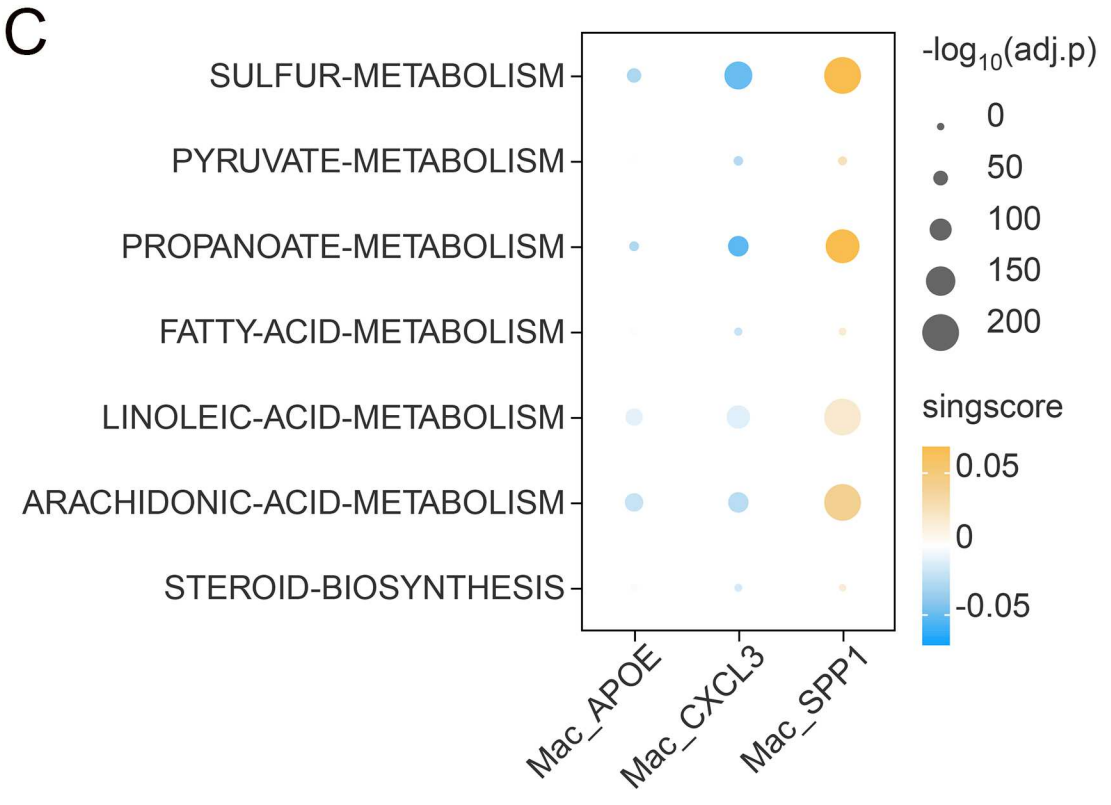
A


Probability
1.0
0.8
0.6
0.4
0.2
0.0
Expression
low
high
HR = 1.58 (1.27 − 1.98)
logrank P = 4.9e−05
0
20
40
60
80
Time (months)
Number at risk
low 1943 1901 1556 787 43
high 1033 1001 764 357 24

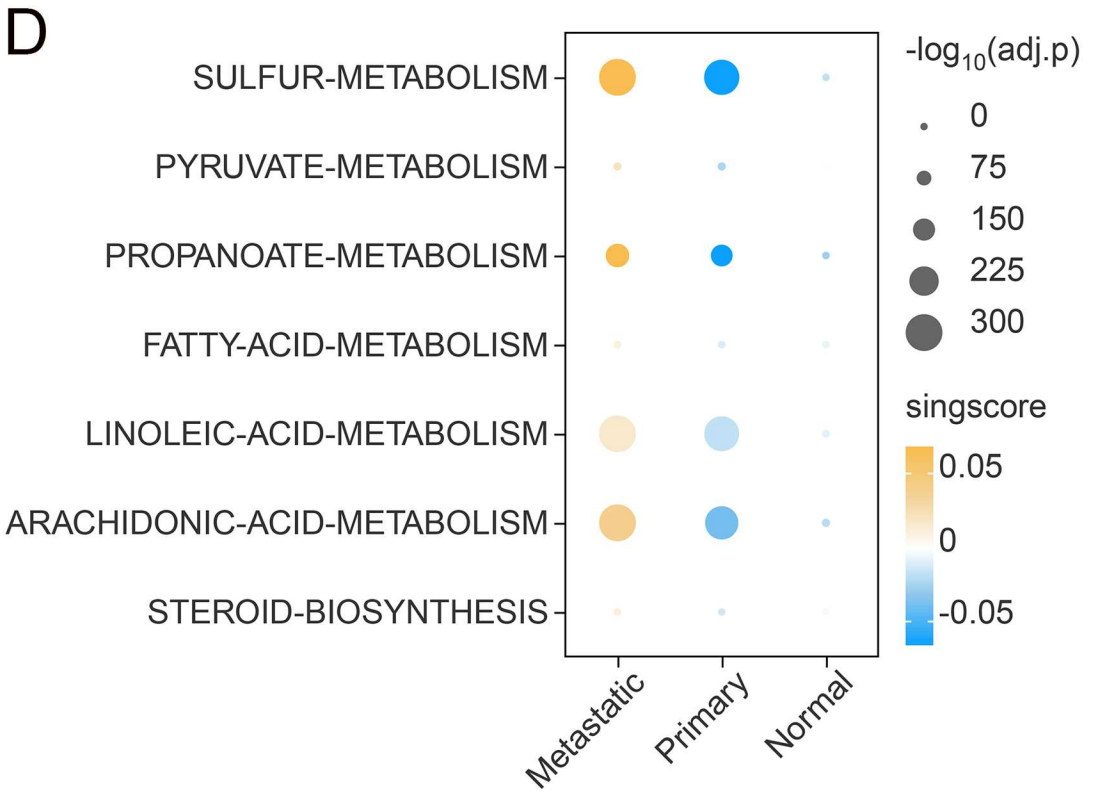
B


E4F1(+)
ELF4(+)
ZNF597(+)
CREB3(+)
NFKB2(+)
TFEB(+)
FOXC1(+)
BATF3(+)
NFE2L2(+)
RELA(+)
FOSL2(+)
RELB(+)
MAFF(+)
XBP1(+)
ERG(+)
ATF4(+)
DDIT3(+)
ETS1(+)
ETS2(+)
ATF6B(+)
NFKB1(+)
STAT4(+)
IRF7(+)
REL(+)
SRF(+)
HOXA9(+)
MAF(+)
FOS(+)
ETV6(+)
GABPA(+)
ETV3(+)
JUND(+)
YY1(+)
BHLHE40(+)
Mac_APOE
Mac_CXCL3
Mac_SPP1
z−score
2
1
0
−1
−2

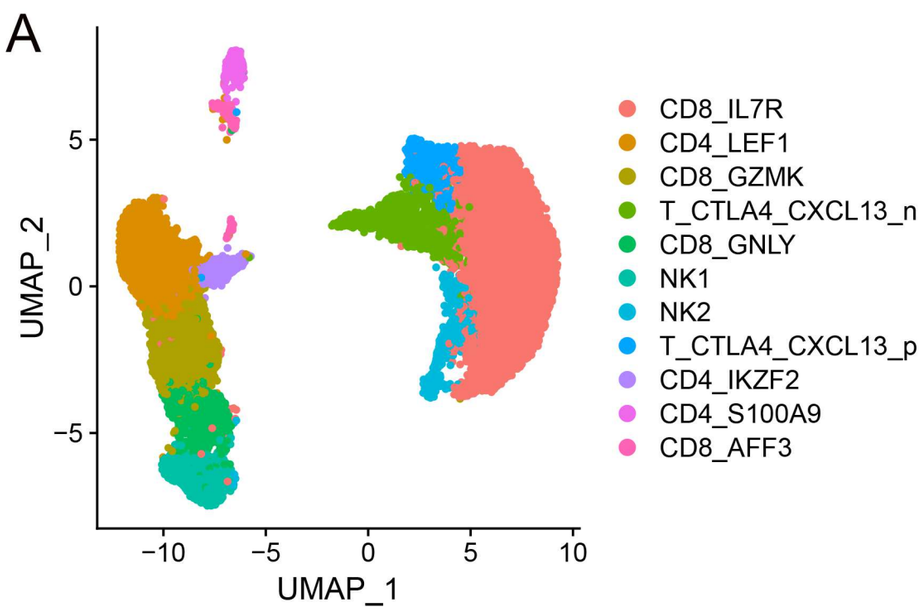
C


SULFUR-METABOLISM
PYRUVATE-METABOLISM
PROPANOATE-METABOLISM
FATTY-ACID-METABOLISM
LINOLEIC-ACID-METABOLISM
ARACHIDONIC-ACID-METABOLISM
STEROID-BIOSYNTHESIS
Mac_APOE
Mac_CXCL3
Mac_SPP1
-log10(adj.p)
0
50
100
150
200
singscore
0.05
0
-0.05

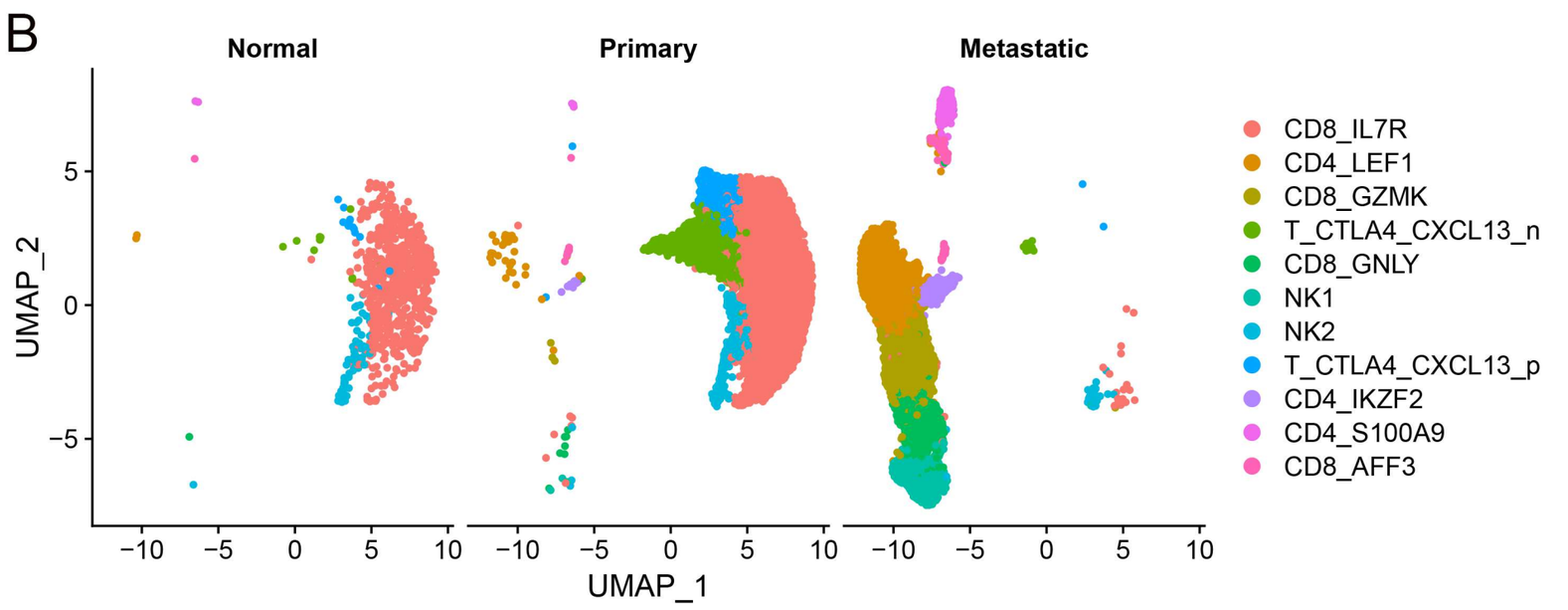
D


SULFUR-METABOLISM
PYRUVATE-METABOLISM
PROPANOATE-METABOLISM
FATTY-ACID-METABOLISM
LINOLEIC-ACID-METABOLISM
ARACHIDONIC-ACID-METABOLISM
STEROID-BIOSYNTHESIS
Metastatic
Primary
Normal
-log10(adj.p)
0
75
150
225
300
singscore
0.05
0
-0.05

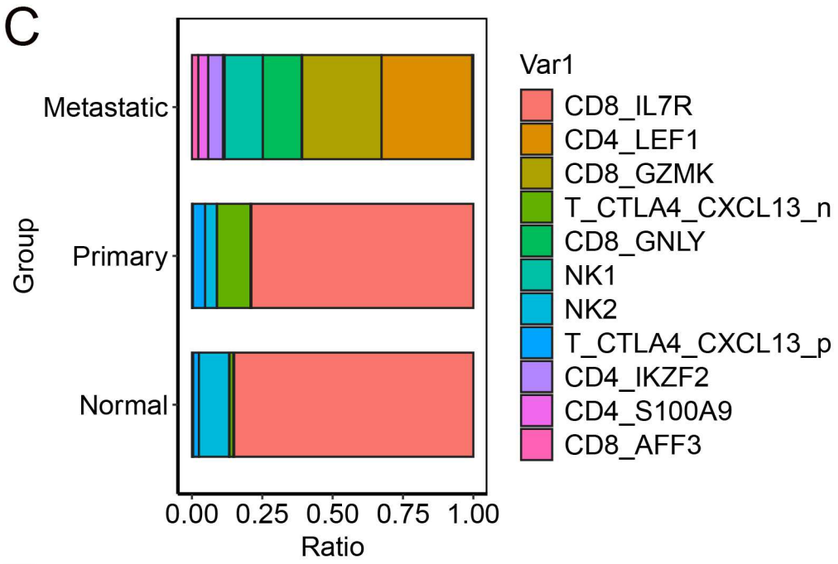
A



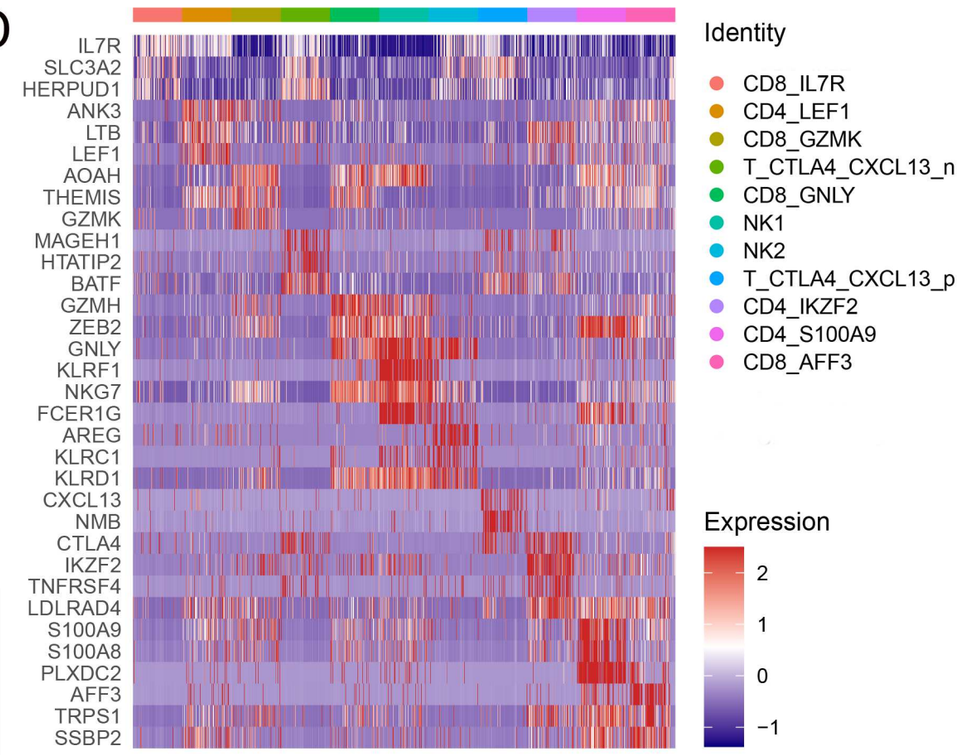
B



C

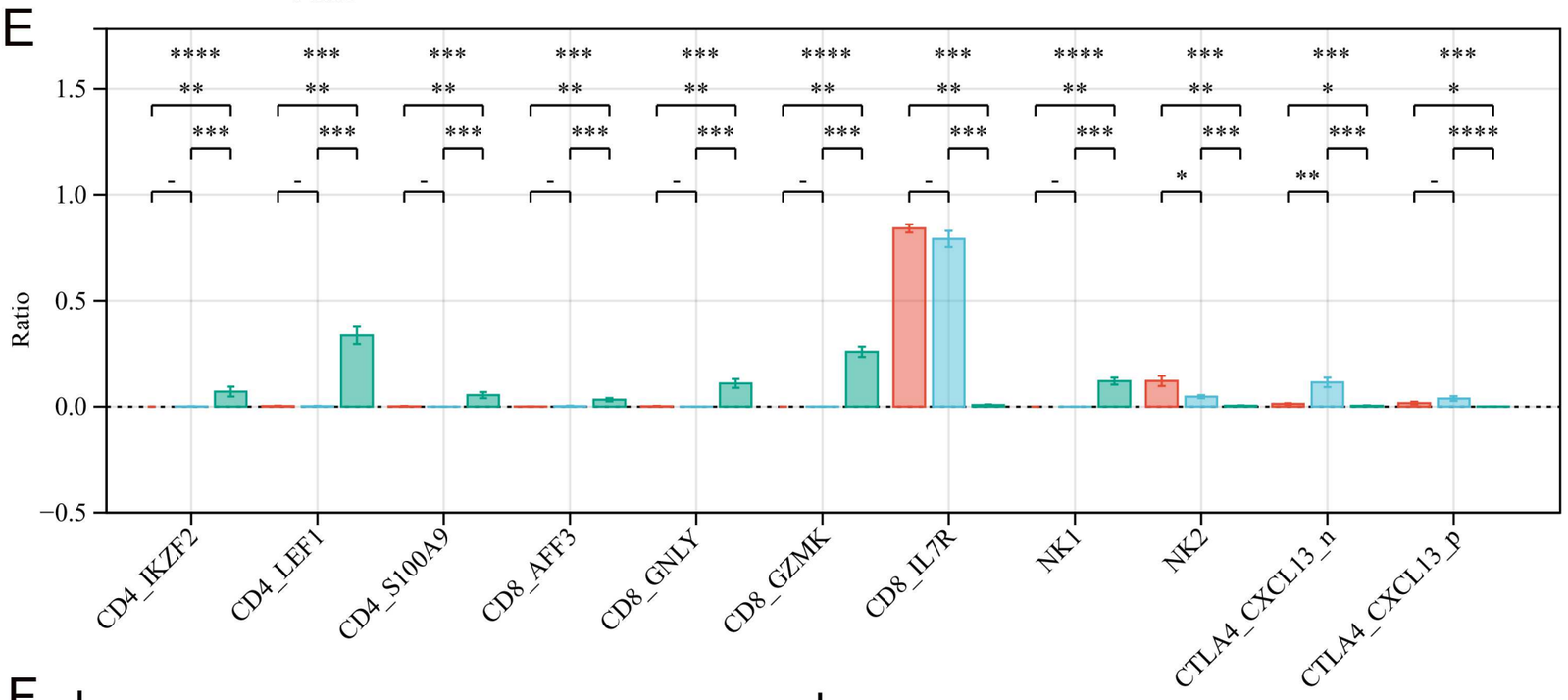


D

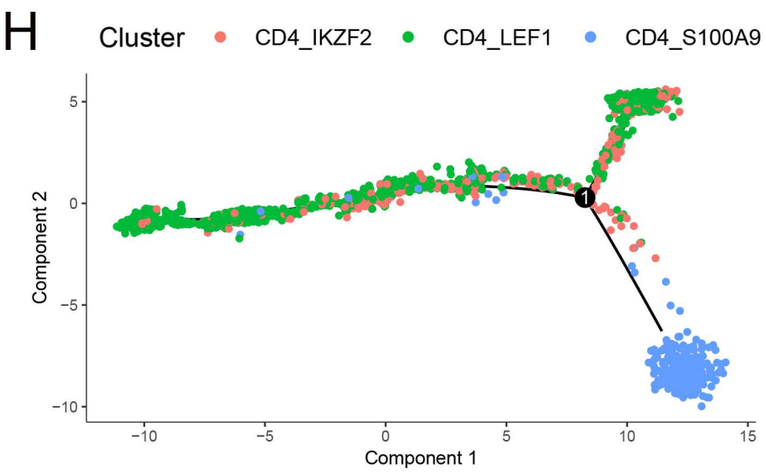


Group
Normal
Primary
Metastatic

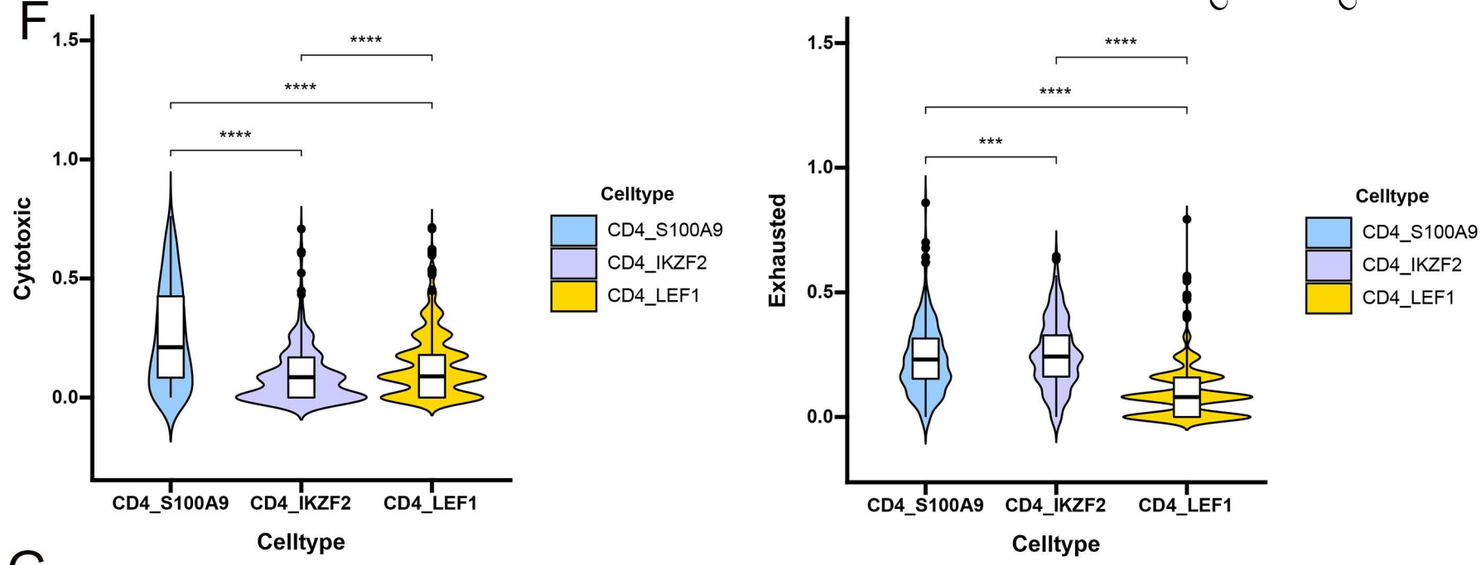
E

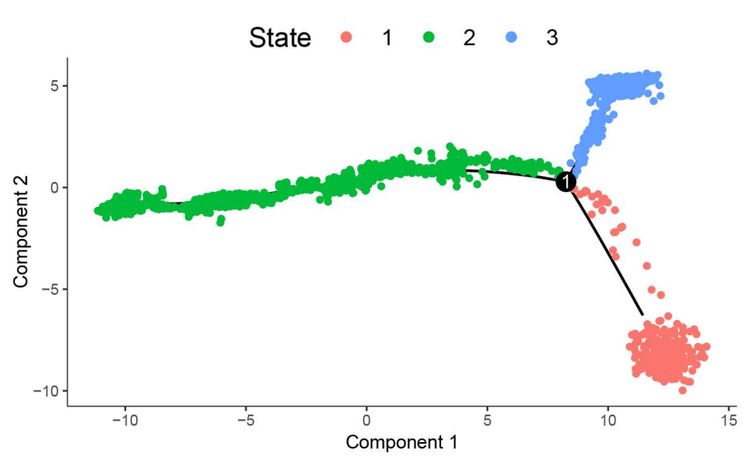


H

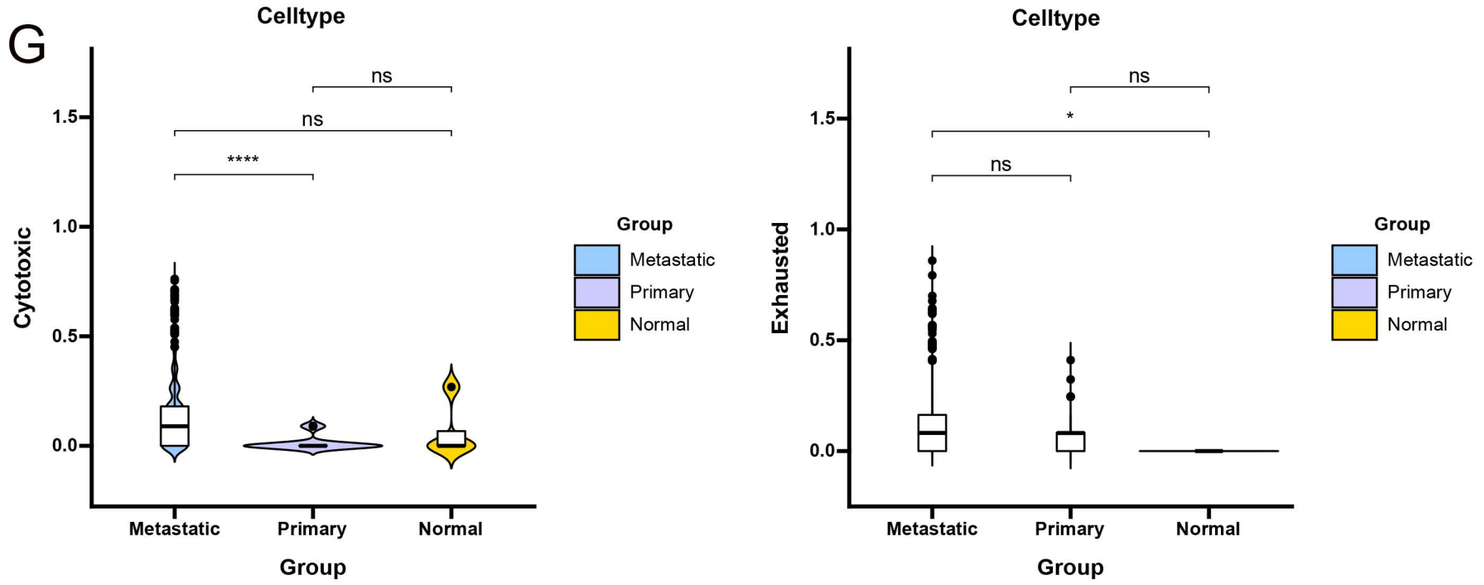


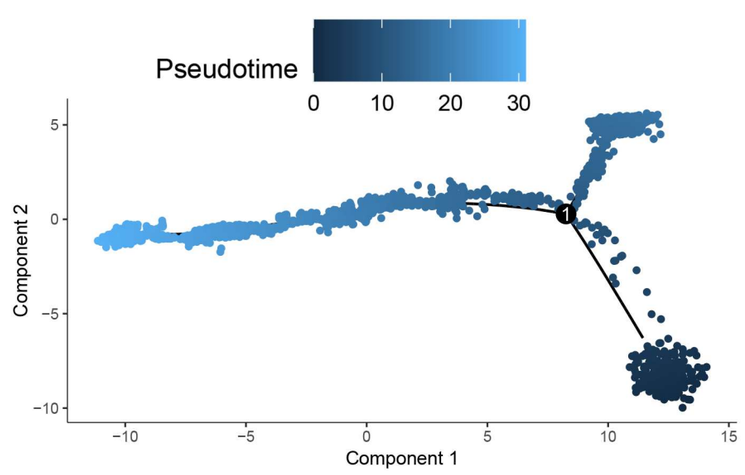
F



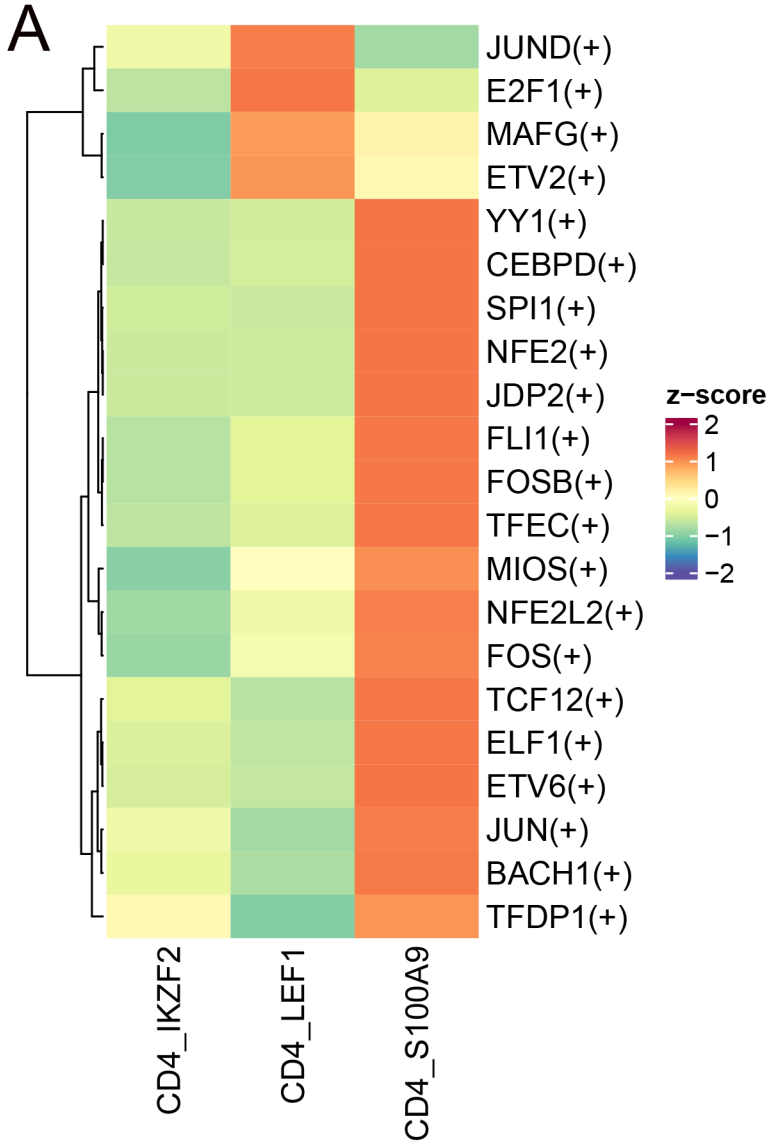


G

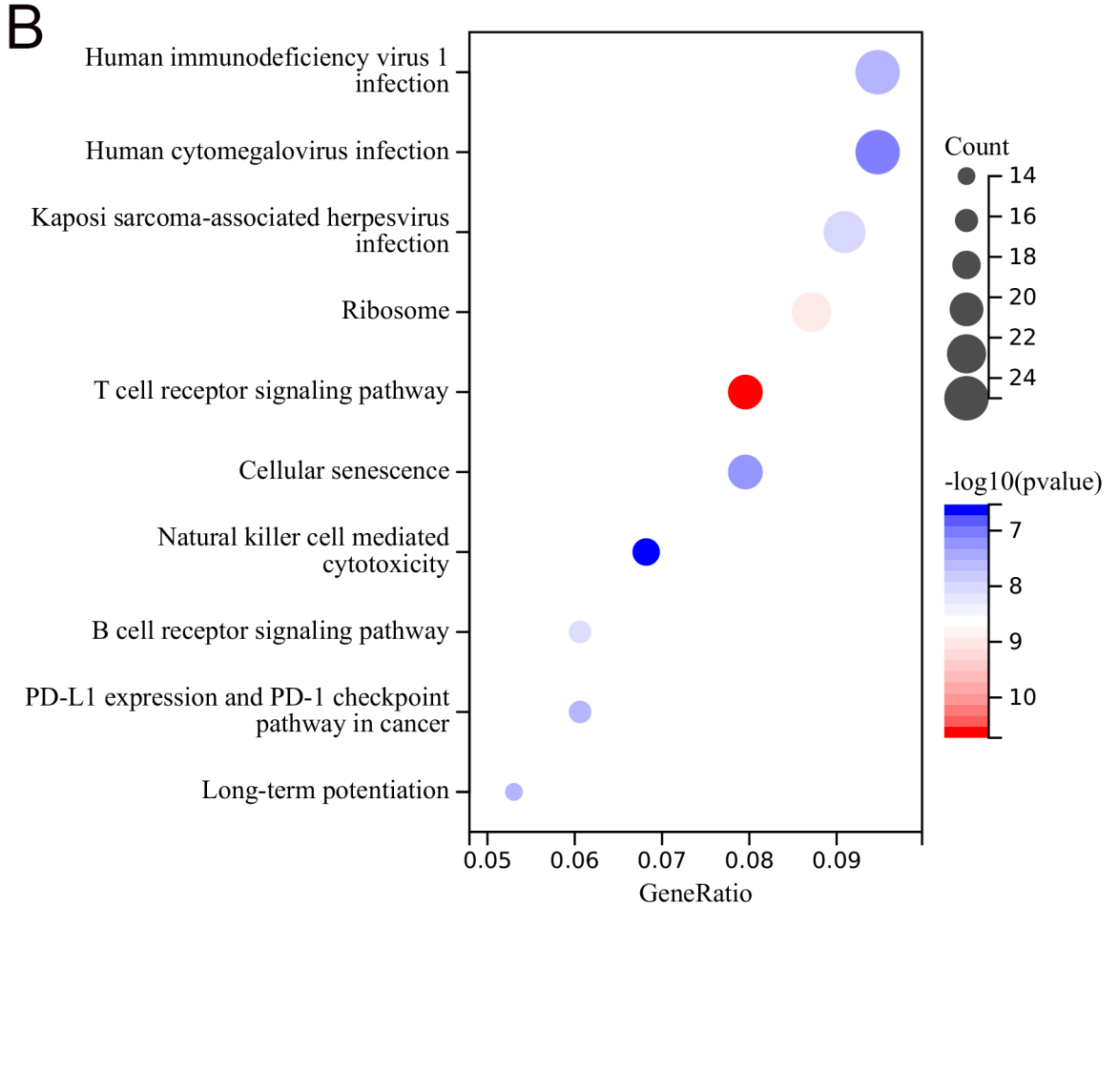




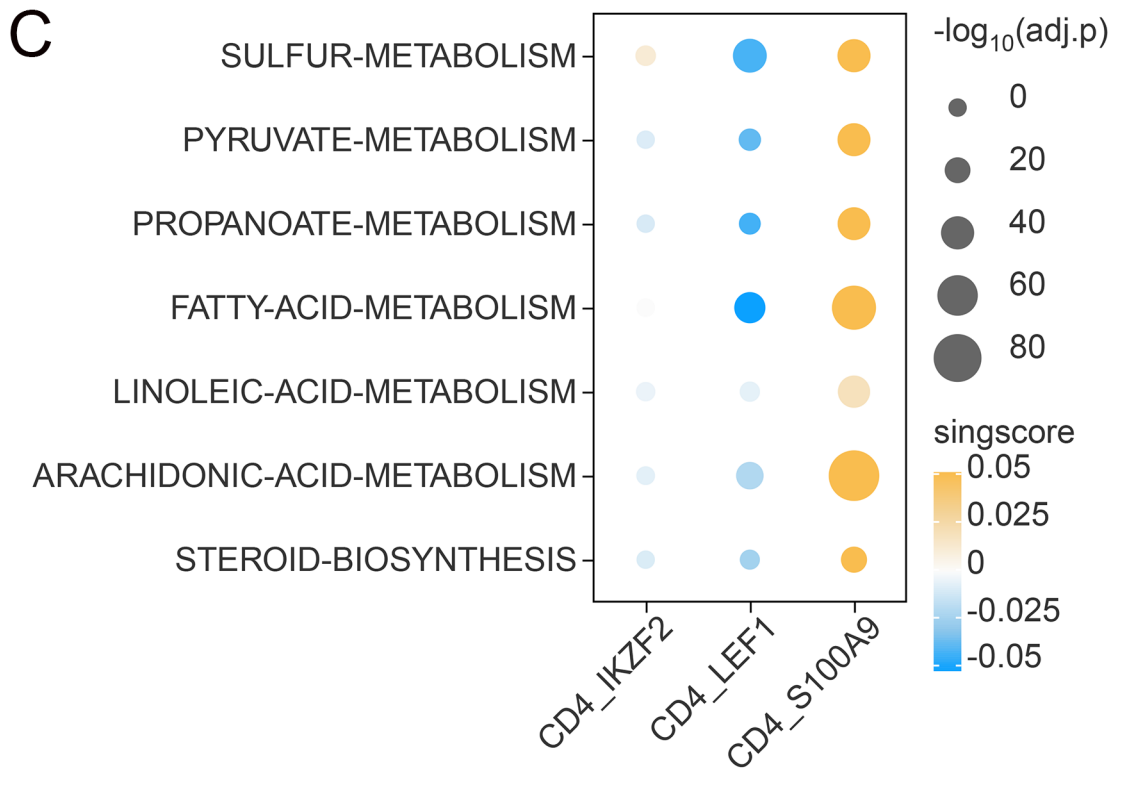
A


JUND(+)
E2F1(+)
MAFG(+)
ETV2(+)
YY1(+)
CEBPD(+)
SPI1(+)
NFE2(+)
JDP2(+)
FLI1(+)
FOSB(+)
TFEC(+)
MIOS(+)
NFE2L2(+)
FOS(+)
TCF12(+)
ELF1(+)
ETV6(+)
JUN(+)
BACH1(+)
TFDP1(+)
z−score
2
1
0
−1
−2
CD4_IKZF2
CD4_LEF1
CD4_S100A9

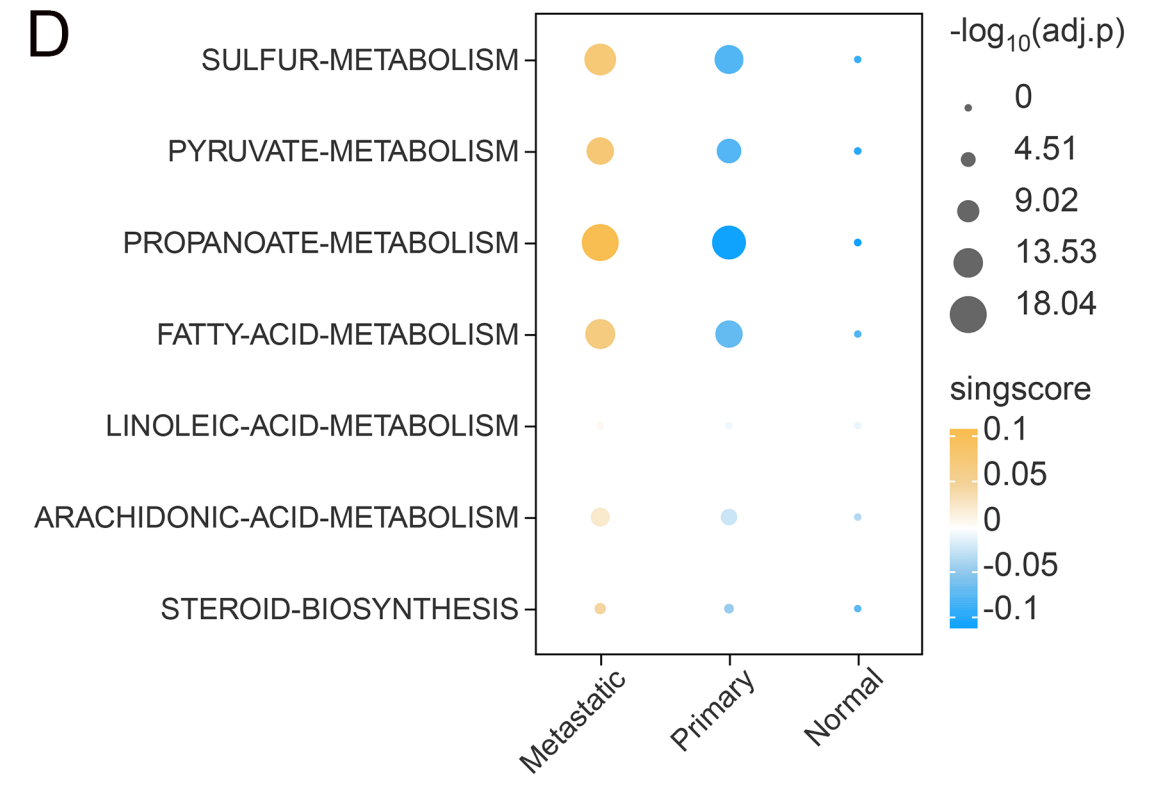
B

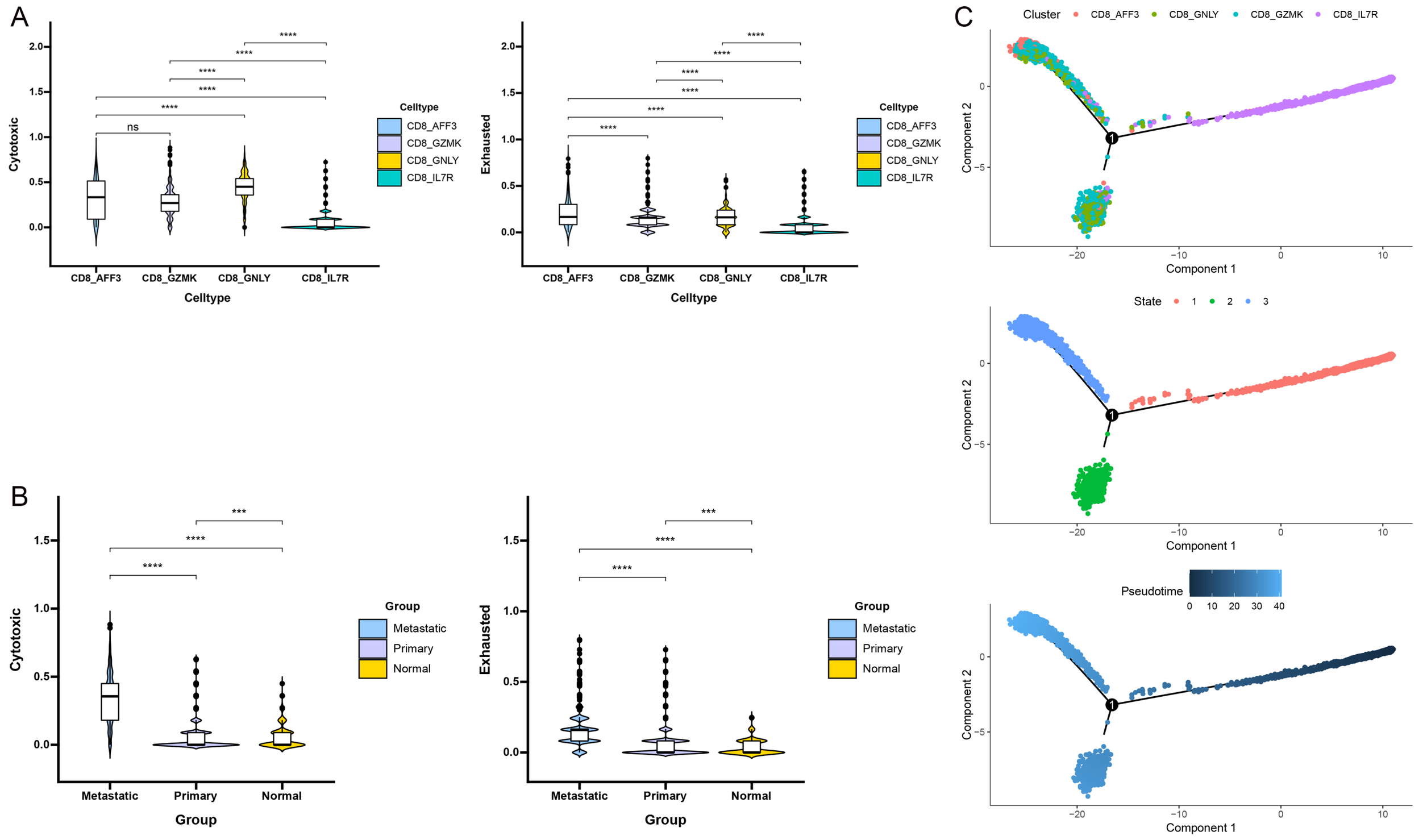

Human immunodeficiency virus 1 infection
Human cytomegalovirus infection
Kaposi sarcoma-associated herpesvirus infection
Ribosome
T cell receptor signaling pathway
Cellular senescence
Natural killer cell mediated cytotoxicity
B cell receptor signaling pathway
PD-L1 expression and PD-1 checkpoint pathway in cancer
Long-term potentiation
0.05
0.06
0.07
0.08
0.09
GeneRatio
Count
14
16
18
20
22
24
-log10(pvalue)
7
8
9
10

C

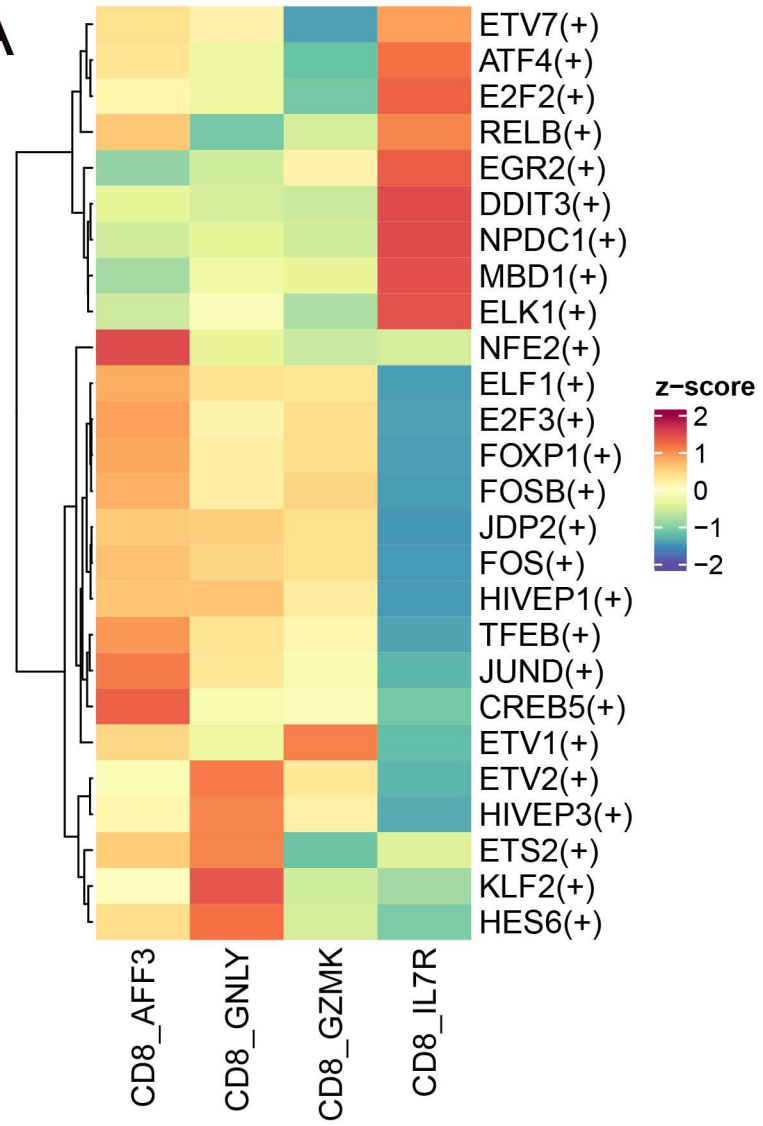

SULFUR-METABOLISM
PYRUVATE-METABOLISM
PROPANOATE-METABOLISM
FATTY-ACID-METABOLISM
LINOLEIC-ACID-METABOLISM
ARACHIDONIC-ACID-METABOLISM
STEROID-BIOSYNTHESIS
CD4_IKZF2
CD4_LEF1
CD4_S100A9
-log10(adj.p)
0
20
40
60
80
singscore
0.05
0.025
0
-0.025
-0.05

D

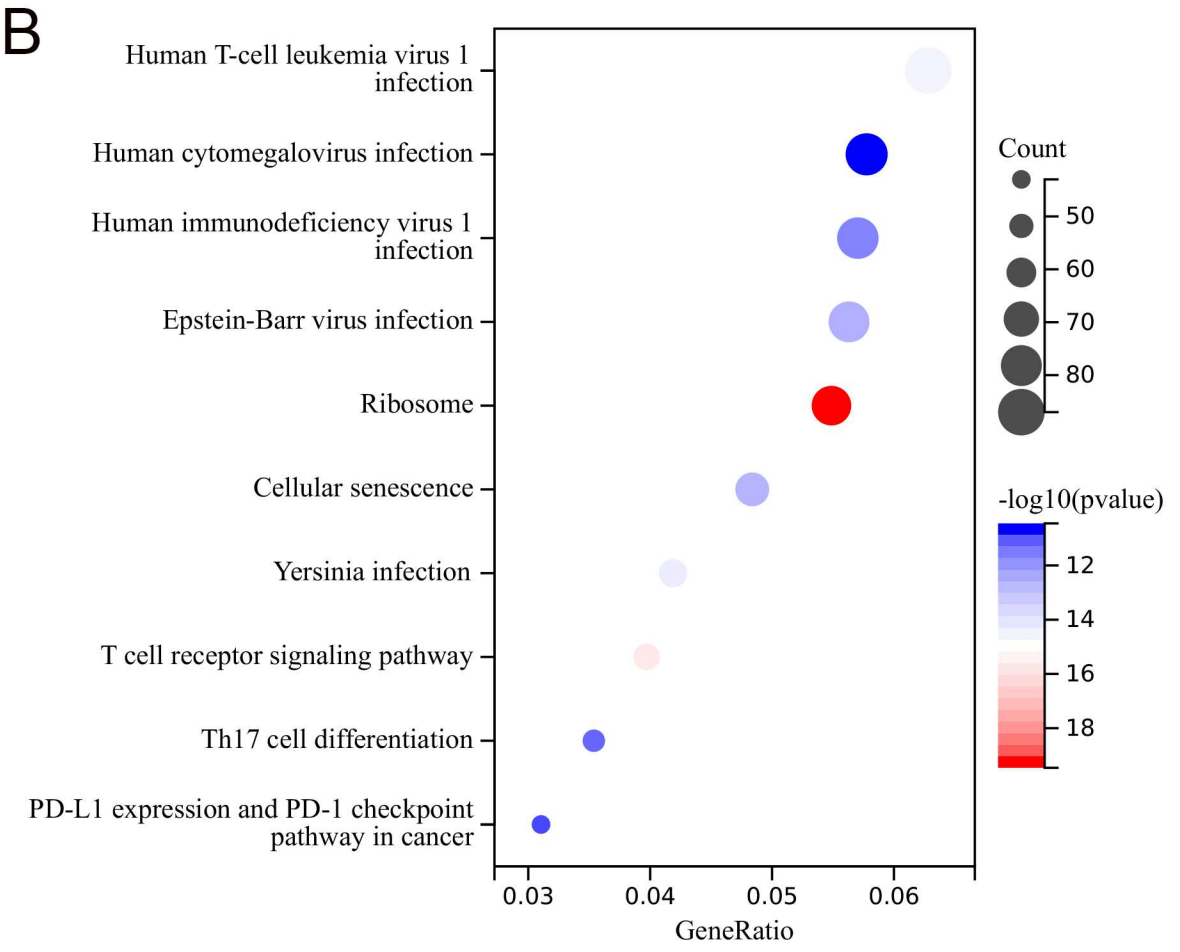

SULFUR-METABOLISM
PYRUVATE-METABOLISM
PROPANOATE-METABOLISM
FATTY-ACID-METABOLISM
LINOLEIC-ACID-METABOLISM
ARACHIDONIC-ACID-METABOLISM
STEROID-BIOSYNTHESIS
Metastatic
Primary
Normal
-log10(adj.p)
0
4.51
9.02
13.53
18.04
singscore
0.1
0.05
0
-0.05
-0.1


A
Cytotoxic
Exhausted
ns
****
Celltype
CD8_AFF3
CD8_GZMK
CD8_GNLY
CD8_IL7R
B
***
Group
Metastatic
Primary
Normal
C
Cluster
State
Pseudotime
Component 1
Component 2

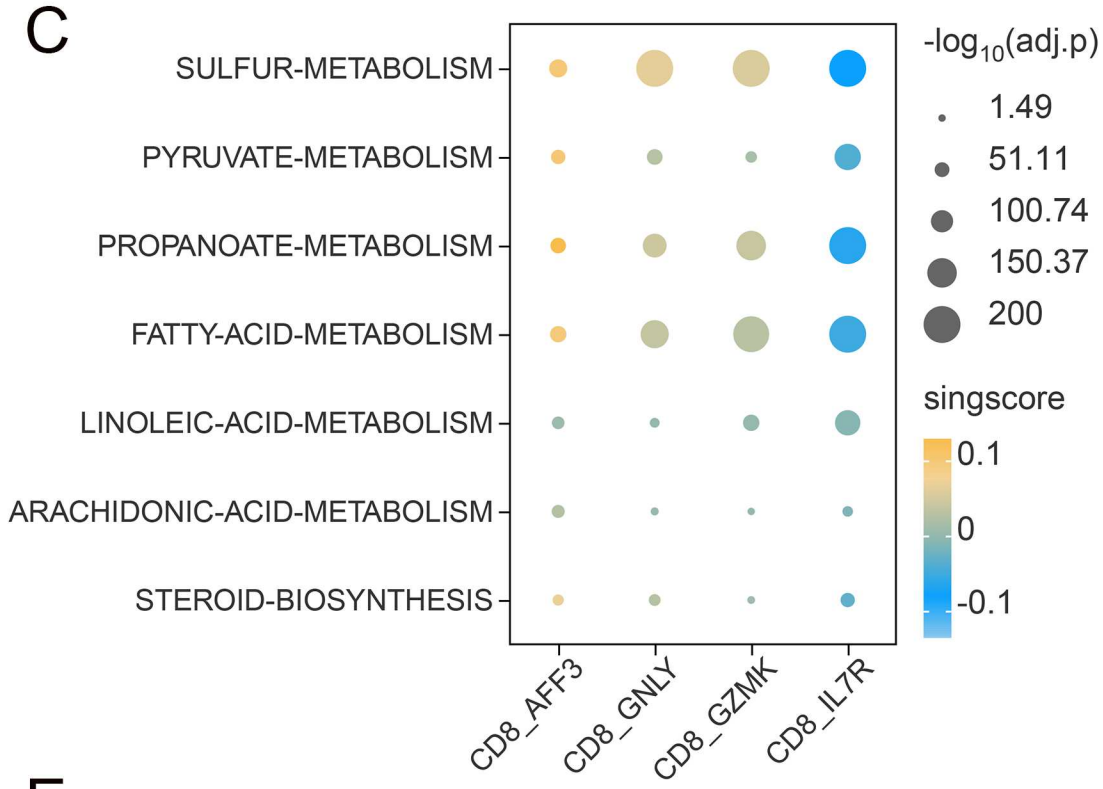
A


ETV7(+)
ATF4(+)
E2F2(+)
RELB(+)
EGR2(+)
DDIT3(+)
NPDC1(+)
MBD1(+)
ELK1(+)
NFE2(+)
ELF1(+)
E2F3(+)
FOXP1(+)
FOSB(+)
JDP2(+)
FOS(+)
HIVEP1(+)
TFEB(+)
JUND(+)
CREB5(+)
ETV1(+)
ETV2(+)
HIVEP3(+)
ETS2(+)
KLF2(+)
HES6(+)
z−score
2
1
0
−1
−2
CD8_AFF3
CD8_GNLY
CD8_GZMK
CD8_IL7R

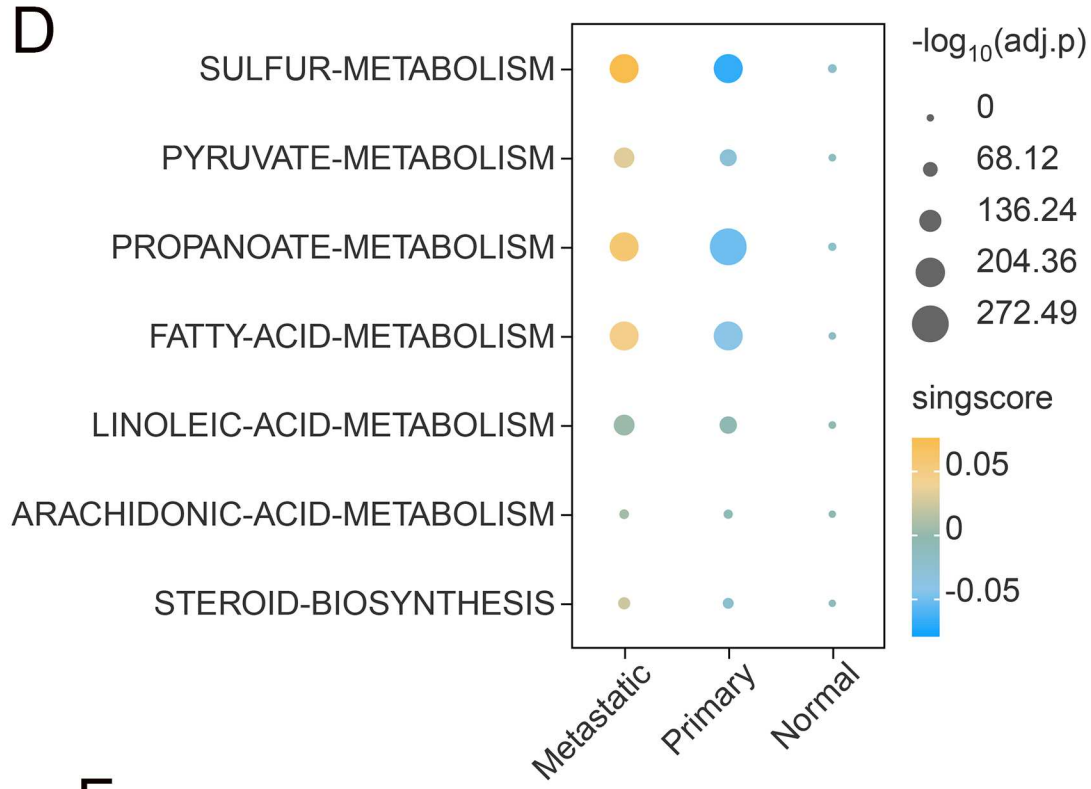
B


Human T-cell leukemia virus 1 infection
Human cytomegalovirus infection
Human immunodeficiency virus 1 infection
Epstein-Barr virus infection
Ribosome
Cellular senescence
Yersinia infection
T cell receptor signaling pathway
Th17 cell differentiation
PD-L1 expression and PD-1 checkpoint pathway in cancer
0.03
0.04
0.05
0.06
GeneRatio
Count
50
60
70
80
-log10(pvalue)
12
14
16
18

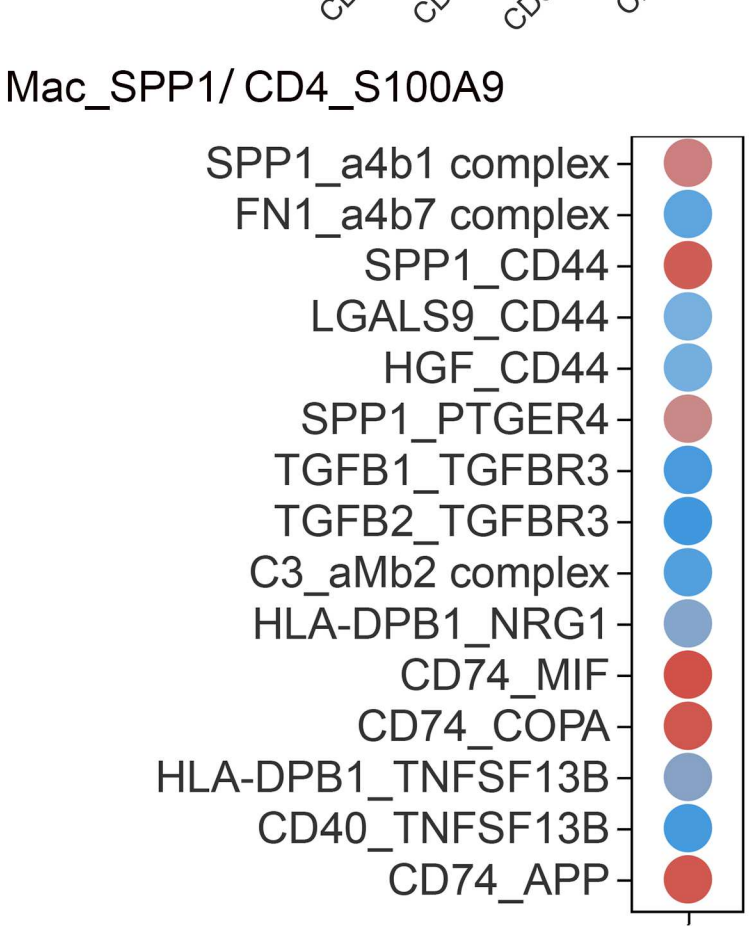
C


SULFUR-METABOLISM
PYRUVATE-METABOLISM
PROPANOATE-METABOLISM
FATTY-ACID-METABOLISM
LINOLEIC-ACID-METABOLISM
ARACHIDONIC-ACID-METABOLISM
STEROID-BIOSYNTHESIS
CD8_AFF3
CD8_GNLY
CD8_GZMK
CD8_IL7R
-log10(adj.p)
1.49
51.11
100.74
150.37
200
singscore
0.1
0
-0.1

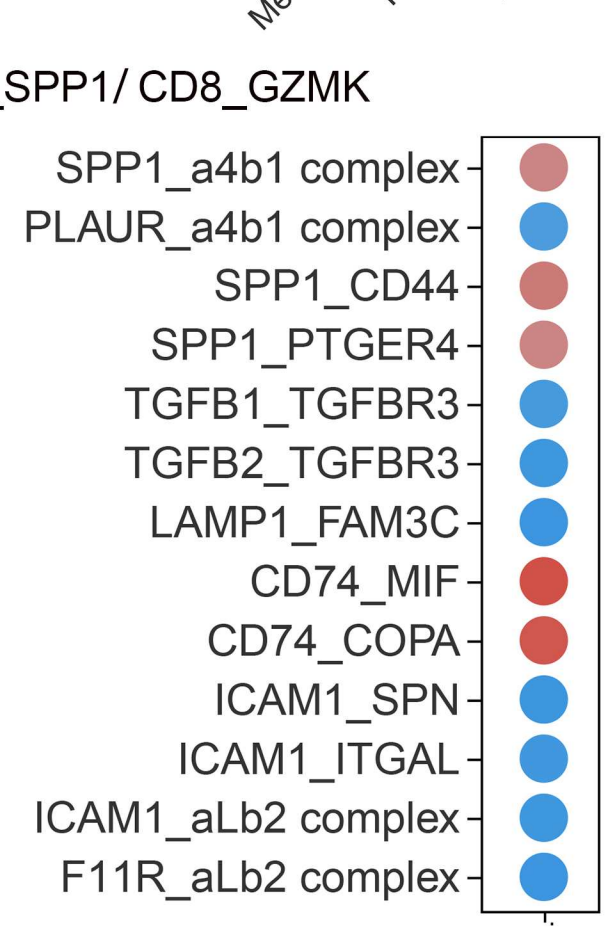
D


SULFUR-METABOLISM
PYRUVATE-METABOLISM
PROPANOATE-METABOLISM
FATTY-ACID-METABOLISM
LINOLEIC-ACID-METABOLISM
ARACHIDONIC-ACID-METABOLISM
STEROID-BIOSYNTHESIS
Metastatic
Primary
Normal
-log10(adj.p)
0
68.12
136.24
204.36
272.49
singscore
0.05
0
-0.05

E


Mac_SPP1/ CD4_S100A9
SPP1_a4b1 complex
FN1_a4b7 complex
SPP1_CD44
LGALS9_CD44
HGF_CD44
SPP1_PTGER4
TGFB1_TGFBR3
TGFB2_TGFBR3
C3_aMb2 complex
HLA-DPB1_NRG1
CD74_MIF
CD74_COPA
HLA-DPB1_TNFSF13B
CD40_TNFSF13B
CD74_APP

F


Mac_SPP1/ CD8_GZMK
SPP1_a4b1 complex
PLAUR_a4b1 complex
SPP1_CD44
SPP1_PTGER4
TGFB1_TGFBR3
TGFB2_TGFBR3
LAMP1_FAM3C
CD74_MIF
CD74_COPA
ICAM1_SPN
ICAM1_ITGAL
ICAM1_aLb2 complex
F11R_aLb2 complex

Supplementary Files

This is a list of supplementary files associated with this preprint. Click to download.

- GraphicalAbstract.tif